AN ANALYTICAL STUDY ON VIBRATION OF RAILWAY WHEELS AND METHODS FOR NOISE REDUCTION

BY

HIROSHI MATSUHISA

1982

AN ANALYTICAL STUDY ON VIBRATION OF RAILWAY WHEELS AND METHODS FOR NOISE REDUCTION

BY

HIROSHI MATSUHISA

1982

CONTENTS

CHAPTER 1 INTRODUCTION

High speed railways have become a very convenient and effective means of transportation for medium range distances. However, its noise and vibration give a great deal of annoyance to the residents along the tracks. Recently, not only the noise by the high speed railways but also the noise by the conventional railways has become a social problem. The noise reduction is regarded to be of prime importance, and many studies on this problem have been carried out so far. However, except noise insulation walls, no effective practical measures for the noise reduction has been found yet.

The noise from railways was measured by many researchers[1-6], and it was found that the noise is generated predominantly by the vibration of the wheels and the rails. When a train is traversing on tight curves, transverse vibration of the wheels is stimulated, and it produces an intense noise[7,8].

The vibration of the wheel has been investigated experimentally and theoretically by many researchers[9-11]. Their theoretical analyses are based on the assumption that the wheels are thin circular plates or rings. However, the effects of the shear deformation and the rotatory inertia on the vibration of the wheel have to be taken into consideration, because wheel's thickness is considerably large compared with its diameter.

Damped wheels[12,13] and resilient wheels[14,15] have been investigated experimentally. They can reduce the noise level by several decibels. However, no theoretical analysis of their vibration has been reported so far. The

resilient wheel is hardly used in practice because of its mechanical strength and cost.

The purpose of the present work is to perform the precise theoretical analysis of the wheels and to construct the low noise wheels, such as spoke wheels and damped wheel.

In chapter 2, the general concept of the vibration and noise caused by the Shinkansen is discussed[16-18]. The author measured the noise and the vibration of ground and houses at two sites along the Shinkansen. Furthermore, human response to the vibration and the noise was investigated by questionnaires distributed among two thousand residents along the tracks. On the basis of the measurements and the questionnaires, the outline of the practical vibration and the noise is manifested.

In chapter 3, the theoretical analysis of the transverse vibration of the wheel is discussed[19,20]. First, we deal with a thin wheel. Since the wheel contacts with the rail, in the analysis, the wheel is assumed to be simply supported at one point on its periphery. Second, the web wheel which is composed of a hub, a web, and a rim is dealt. The rim is considerably thick compared with its diameter, so the effects of the shear deformation and rotatory inertia are taken into consideration. The web wheel is assumed to be a circular plate with a stepped thickness, and its vibration is analyzed theoretically by making use of Mindlin theory[21,22]. Furthermore, laboratory experiments using model wheels are carried out in order to confirm the result of theoretical analysis.

In chapter 4, the relations among the vibration, the noise, the velocity, and the load are investigated by using a laboratory model[23]. Curves of a track are simulated by

a contact angle between a guide wheel and the test wheel in the experimental apparatus, and its effect on the vibration and the noise are also investigated.

In chapter 5, the relation between the vibration and the noise is studied[23]. An acoustic radiation coefficient is defined by the ratio of an acoustic power and a mechanical power of the vibrating wheel. The acoustic radiation coefficients of the vibration of normal modes are calculated. The characteristics of the wheel's sound radiation are discussed by means of this coefficient.

In chapter 6, the coupled vibration of the web wheel and a rail is studied[24]. In this study, the emphasis is placed on the vibration of the wheel. Therefore for the sake of simplification, the rail is simulated by a beam with free ends, and the wheel and the rail are assumed to be connected by a spring. With these assumptions, the coupled vibration is investigated theoretically and experimentally.

In chapter 7, the spoke wheel is investigated[25]. The spoke wheel is expected to radiate less noise than the conventional web wheel because of its small area of sound radiation. The vibration of the spoke wheel is analyzed with an assumption that the rim is elastically supported by springs which simulate the spokes. Furthermore, the noise by the spoke wheel is compared with that by the web wheel, and its effect on the noise reduction is confirmed experimentally.

In chapter 8, the vibration of a damped wheel is investigated[26]. A vibration absorber which is composed of a thin annular steal plate and a rubber, is attached to the main web wheel. The relation between the vibration level

and the structure of the absorber is investigated theoretically and experimentally. Also, the noise reduction by the absorber is investigated by making use of several models of the damped wheel.

REFERENCES

1) Arai,M., & Ban,Y., Proc.Inter-Noise 75 (1975), 69.
2) Nimura,T., et al., Proc.Inter-Noise 75 (1975), 93.
3) Rathe,E.J., J.Sound & Vibration, 51-3 (1977), 371.
4) Baker,C.J., et al., J.Sound & Vibration, 64-4 (1979), 589.
5) Lotz,R., J.Sound & Vibration, 51-3 (1977), 319.
6) King,W.F. & Bechert,D., J.Sound & Vibration, 66-3 (1979), 311.
7) Stüber,C., J.Sound & Vibration, 43-2 (1975), 281.
8) Rudd,M.J. J.Sound & Vibration 46-3 (1976), 381.
9) Remington,P.J., J.Sound & Vibration, 46-3 (1976), 359.
10) Arai,H., et al. Proc.JSME 760-14 (1976), 92.
11) Yokose,K., Railway Technical Research Report, Japanese National Railway, No.1071 (1978).
12) Raquet,E., Rail Engineering International, January-March (1980), 13.
13) Satoda,K., et al., Sumitomo Kinzoku, 29-1 (1977), 68.
14) Vér,I.L., et al., J.Sound & Vibration, 46-3 (1976), 395.
15) Matsumiya,S., & Sugawara,S., Sumitomo Kinzoku, 26-2 (1974), 97.
16) Shibata,T., et al., "Report of Pollusion by the Shinkansen at Takatsuki-city" (1975).

17) Matsuhisa,H., & Shibata,T., Proc.Inter-Noise 75 (1975), 101.
18) Shibata,T., & Matsuhisa,H., Proc.Inter-Noise 75 (1975), 113.
19) Susumu,S., & Matsuhisa,H., Bull.JSME, 21-160 (1978), 1475.
20) Matsuhisa,H., et al., Bull.JSME, 24-191 (1981), 849.
21) Mindlin,R.D., J.Apple.Mech., 18 (1951), 31.
22) Mindlin,R.D. & Deresiewicz,H., J.Appl.Phys., 25-10 (1954), 1329.
23) Matsuhisa,H., & Sato,S., Bull.JSME, 22-173 (1979), 1626.
24) Matsuhisa,H., et al., Proc.JSME, 815-2 (1981), 51.
25) Matsuhisa,H., et al., Proc.JSME, 824-9 (1982), 25.
26) Sato,S., et al., Proc.JSME, 827-2 (1982), 100.

CHAPTER 2 GENERAL CONCEPTS OF VIBRATION AND NOISE GENERATED BY THE SHINKANSEN

2.1 Introduction

The Shinkansen opened a new era in railway service for mass passenger transportation with high speed in 1964. It has become a very convenient and effective means of transportation for medium range distances. However, its vibration and noise have given a great deal of annoyance to the residents along the tracks and have even become a social problem. The problem has turned so serious that a case was brought to court in Nagoya district. However, it is not easy to find the general concepts of the noise and the vibration, because they are influenced by many factors, such as the structure of the tracks, the surface condition of the rails, and the train speed. Concerning the noise reduction, no effective measure has been found other than a noise insulation wall.

The author measured the vibration and the noise caused by the Shinkansen at two sites, Takatsuki-shi in Osaka prefecture and Seta-cho in Shiga prefecture in 1974[1,2,3]. Also, human response to the vibration and the noise was investigated by questionnaires distributed among two thousands residents along the tracks. In this chapter, the outlines of the vibration and the noise by the Shinkansen is discussed on the basis of the measurements and the questionnaires.

2.2 Sources of Vibration and Noise

In order to study the train noise, first of all, we have to know their sources[4,5,6]. Figure 2-1 shows an example of spacial distribution of the noise generated by the Shinkansen's train running on an elevated track[7]. The noise sources are the rolling devices (wheels and rails), the driving devices (traction motors and gears), the auxiliary equipments (cooling fans, compressors and generators), and power collection system (pantograph sliders and trolly wires). Also, a high velocity car body is expected to produce aerodynamic noise.

Among them, the most intense noise source is supposed to be the rolling devices. The rolling noise is caused by collisions and frictions of the wheels and rails. When the rails have wave form wear or the wheels have tire flat, the noise of the high speed train increases by 20 dB. This shows that the noise from the rolling devices is very large. The other noise sources are negligible compared with the rolling devices. For example, the trains with and without the driving devices do not have significant difference in the generated noise levels. The auxiliary equipments are the only noise sources at stop, but their contributions become negligible during high speed running. Therefore, when we try to reduce the train noise, the rolling devices should be first taken into consideration. By many studies, it is already known that when a train is on a straight track, the rails are the major noise source; and when a train is on a curve, the wheels are the major noise source.

The vibration is also generated by the interactions of

rails and wheels. Then, the vibration is transmitted to the ground through ties and bed of the track.

2.3 Vibration

Among the factors which are the sources of disturbance to people living along railways are train-induced noise and vibration of buildings. Both noise and vibration may be directly experienced as unpleasant sensations, and vibration can further disturb people because of fears of damage to the building fabric.

Building vibration induced by train is caused by ground vibration originating from the interaction of wheels and rails. There are the ties, the bed, and the ground in the vibration propagation path between the rails and buildings. Those factors have a large effect on the characteristics of the vibration. In this section, in order to know the outlines of the vibration, some general characteristics of the vibration caused by the Shinkansen are briefly discussed from the measured data at Takatsuki and Seta.

The ground vibration has three directions; vertical to the ground, parallel and perpendicular to the track. Just below an elevated track, the vertical vibration is greater than the others, but at far places, all the vibrations have almost the same amplitudes.

Figure 2-2 shows the relation between the vertical vibration velocity and the distance from the track. The data exhibit considerable scatter, but by making use of the least square method, this relation is represented as

$$v = 0.17\ L^{-0.6} \qquad (2\text{-}1)$$

where, v is the vibration velocity (cm/sec) and L is the distance (m).

Concerning the other characteristics, measured data have a large amount of scatter. However, the following tendencies can be observed.

i) The vibration spectrum has two peaks at 2-3 Hz and 40-60 Hz. The vibration at the lower peak frequency decreases when the distance increases.

ii) A track elevated by concrete posts has larger vibration than that on an embankment. This is due to the high damping factor of the soil of the embankment.

iii) The vibration is considerably reduced by a river which lies across the propagation path.

iv) In a wooden house, the indoor vibration is greater than the ground vibration. Also, the vibration of the second floor is greater than that of the first floor. This is due to the resonance of the building.

v) In a ferro-concrete building, the vibration of the first floor is as large as that of the ground. The vibration in the building increases with the floor level.

2.4 Noise

Figure 2-3 shows an example of the relation between the noise level (A scale) and the distance from the track with and without the noise insulation wall. As seen in this figure, the insulation wall reduces the noise from the train on the near side track but does not reduce the noise from the far side track. The noise at places more than 30 meters away from the track is not reduced by the insulation

wall. Figure 2-4 shows the frequency spectra of sound pressure. The components of the sound pressure are lower than several thousands Hz, and there is no sharp peak. However, when a train is traversing on curves, the noise has peaks at the natural frequencies of the transverse vibration of the wheel. The noise in the lower frequency range (below 500 Hz) is not reduced by the insulation wall as seen in this figure. This frequency dependence is explained by sound wave diffraction, reflection, and the noise generated by the vibration of the insulation wall.

Figure 2-5 shows the relationship between the noise level and the train speed. The measurement was carried out at a plane ground covered with grass. In this figure, the straight lines show the approximate relation obtained by the least squares method. Comparing the slopes of these lines, we can see that at an area near the track, the noise can not be decreased by reducing the train speed as much as at an area far from the track. By decreasing the train speed from 200 km/h to 133 km/h, the noise at the areas 100, 200, and 400 meters away from the track decreases by 2, 4, and 5 dB(A), respectively. Therefore, at a near area where the noise is large, it is impossible to have a comfortable living condition, even if the train speed is reduced.

There are two kinds of rail foundation, namely, the stone ballast bed and the slab bed. The noise from the track with the stone ballast bed is smaller than that with the slab bed by about 6 dB. This is due to the high damping factor of the stone ballast bed. New Tokaido Line mainly uses the stone ballast bed, and about a half of new Sanyo Line uses the slab bed. The new lines under construc-

tion will mainly use the slab bed for the sake of easy maintenance, but the stone ballast bed should be used from the viewpoint of the noise reduction.

The indoor noise depends on the location and the structure of the house. However, in general the indoor noise is less than the outdoor noise by several dB(A). Also, when windows are closed, the noise is reduced by 10 to 15 dB(A).

2.5 Damages by Vibration and Noise

Effects of the vibration and noise on houses and health of the residents were investigated by means of the questionnaire.

The vibration makes furniture in the houses rattle, and causes the failure of fitting, cracks in the wall, and failure of the roof in a long time. Figure 2-6 shows the relation between these damages and the distance. As shown in this figure, the shorter the distance is, the higher the ratio of the damage becomes. Wooden houses have about twice as much damage as the ferro-concrete houses. As much as 75 % of the houses within 10 meters of the track were reported to have damages.

The residents who are influenced by the noise and the vibration complained that they "feel noisy", or "are not able to concentrate", or " have a headache". Figure 2-7 and 2-8 show the relations between the health damages and the distance. As shown in Fig. 2-7, it is remarkable that 60 to 75 % of people who live close to the track suffer from headache. Since women stay at home for a longer time than men, they have a higher ratio of the complaint.

The complaint against the vibration is as much as that against the noise. Usually we have been interested in the noise more than the vibration. However, when we deal the train-induced pollution, not only the noise but also the vibraiton should be taken into consideration.

2.6 Conclusions

In this chapter, the practical vibration and noise by the Shinkansen are briefly discussed. Residents along the tracks have been suffering from both the noise and the vibration. Considering the results of the investigation by the questionnaire, we can conclude that the area within 100 meters from the tracks is not suitable for living.

Concerning the preventive measures for vibration and noise, only the noise insulation wall is used in practice. The insulation wall can reduce the noise at the areas very close to the track by a few decibels (A), and we can not expect the insulation wall to have enough effect on the noise reduction.

REFERENCES

1) Shibata,T., et al., "Report of Pollusion by the Shinkansen at Takatsuki-city" (1975).
2) Matsuhisa,H., & Shibata,T., Proc.Inter-Noise 75 (1975), 101.
3) Shibata,T., & Matsuhisa,H., Proc.Inter-Noise 75 (1975), 113.
4) Hemsworth,B., J.Sound & Vibration, 66-3 (1979), 297.

5) Arai,M., & Ban,Y., Proc.Inter-Noise 75 (1975), 69.

6) Nimura,T., et al. Proc.Inter-Noise 75 (1975), 93.

7) Matsui,M., "Technology of Noise Reduction and its Examples", Fuji Technosystem, (1974), 94.

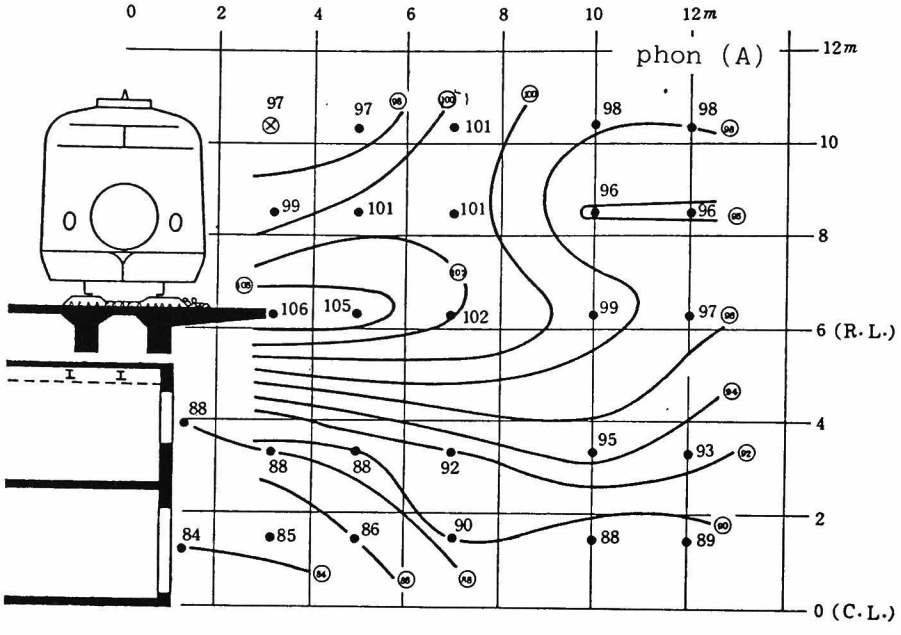

Fig. 2-1 Spacial distribution of the noise generated by the Shinkansen train running on an elevated track (source; Refference 7).

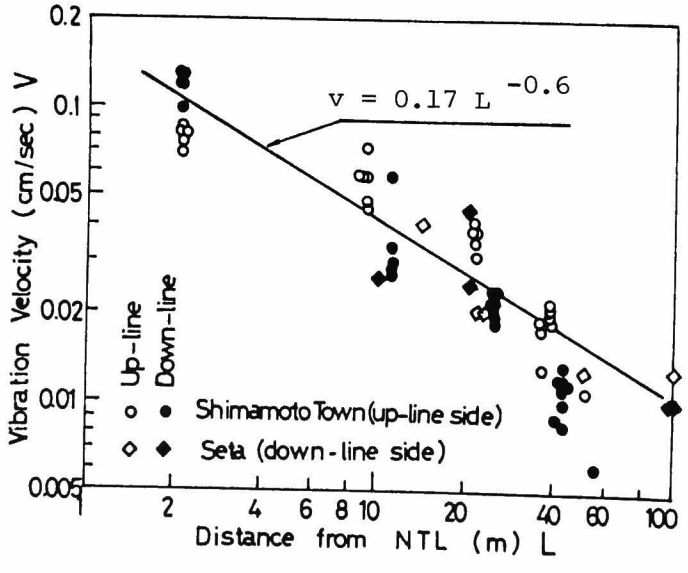

Fig. 2-2 Relation between the vibration velocity and the distance from the track.

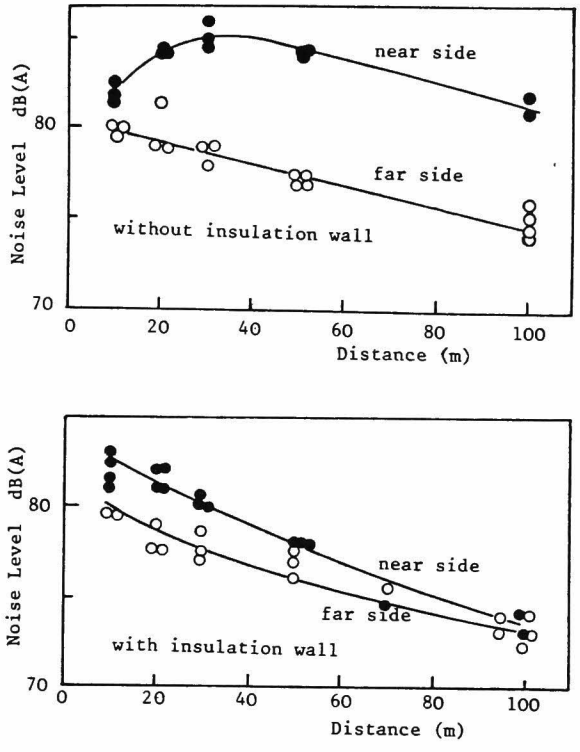

Fig. 2-3 Relation between the noise level and the distance from the track.

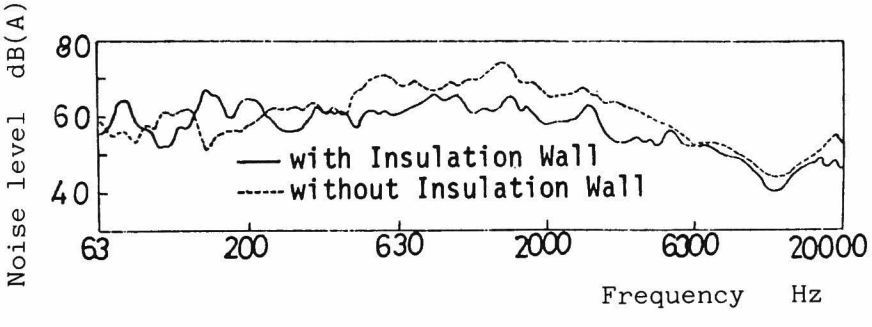

Fig. 2-4 Frequency spectra of the noise.

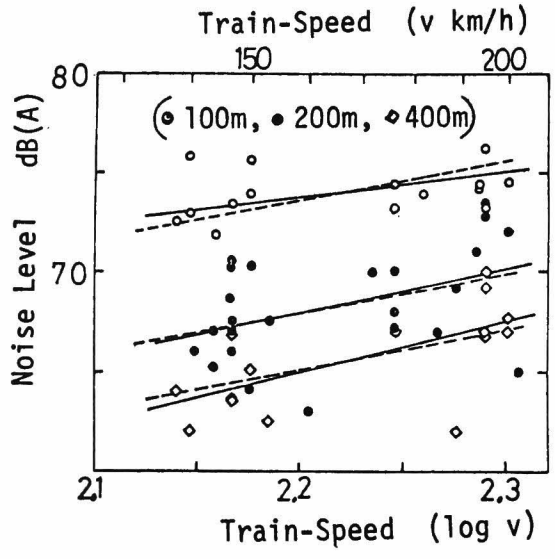

Fig. 2-5 Relation between the train speed and the noise level; solid lines represent the estimated relations at each distance, and broken lines represent their average.

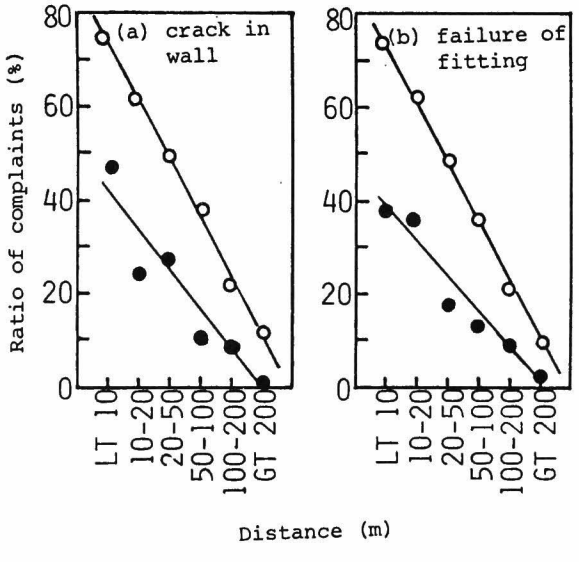

Fig. 2-6 Relation between the damage of houses by the vibration and the distance from the track (o:wooden house, ●:ferro-concrete house).

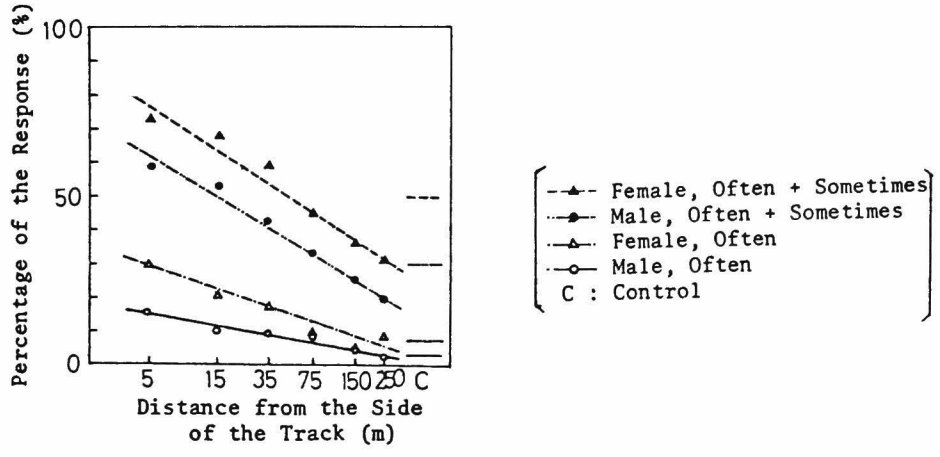

Fig. 2-7 Response to a question "Do you have a headache?".

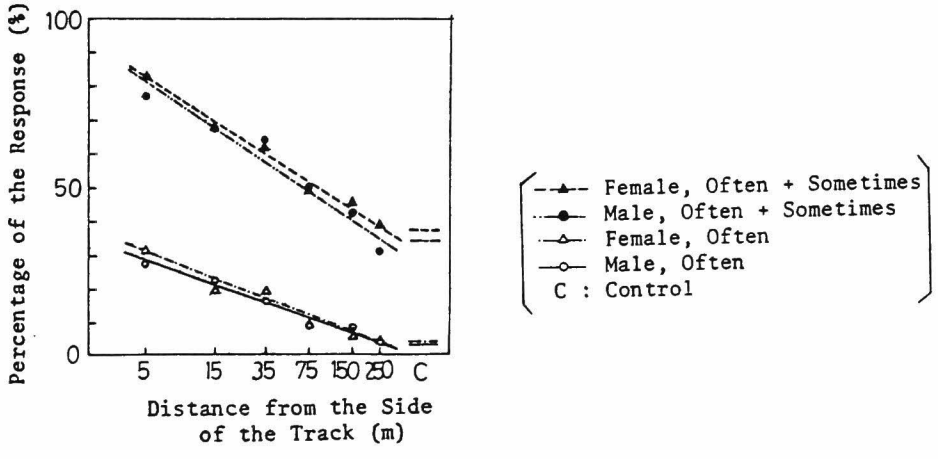

Fig. 2-8 Response to a question "Is your concentration disturbed?".

CHAPTER 3 VIBRATION OF A THIN WHEEL AND A WEB WHEEL

3.1 Introduction

The precise theoretical analysis of the wheel's transverse vibration is studied in this chapter[1,2]. In section 3.2, as the first step, a thin wheel is investigated. The vibration of the thin wheel is analyzed by means of the classical thin plate theory. Since the wheel contacts with a rail, the boudary condition of the contact point should be taken into consideration. Therefore, the thin wheel is assumed to be simply supported at one point on the outer circumference[3,4]. Then, the vibration and the noise caused by a small model of the thin wheel are experimentally investigated.

In section 3.3, the wheel used in the Shinkansen is studied. This wheel is composed of a hub, a web, and a rim, and is referred to as a web wheel. Since the web and the rim have different thickness, the web wheel is assumed to be a circular plate with a stepped thickness. As the rim is considerably thick compared with its diameter, the effects of rotatory inertia and shear deformation are taken into consideration. With these assumptions, the theoretical analysis is carried out. Then, by making use of a model of the web wheel which is 1/6 of that of the Shinkansen's train, the vibration and the noise are experimentally investigated.

3.2 Vibration of a Thin Wheel

3.2.1 Theoretical analysis

In this section, the vibration is assumed to be governed by the small deflections, the effects of rotatory inertia and shear deformation being omitted. The well-known differential equation governing free vibration of a thin homogeneous plate in the cylindrical coordinates (r, θ, z) shown in Fig. 3-1 is

$$D\nabla^4 w - \rho h\omega^2 w = 0 \tag{3-1}$$

where

$$\nabla^2 = \frac{\partial^2}{\partial r^2} + \frac{1}{r}\frac{\partial}{\partial r} + \frac{1}{r^2}\frac{\partial^2}{\partial \theta^2}, \qquad D = \frac{Eh^3}{12(1-\nu^2)}$$

w: transverse deflection, E: Young's modulus, h: plate thickness, ν: Poisson's ratio, ρ: density of the plate.

The general solution of Eq. (3-1) is

$$w(r,\theta)=\{AJ_m(kr)+BY_m(kr)+CI_m(kr)+FK_m(kr)\}\cos m(\theta-\alpha). \tag{3-2}$$

$$k^4 = \rho\omega^2/D, \tag{3-3}$$

in which J_m and Y_m are Bessel functions of the first and second kinds of m-th order, and ω is the angular frequency. I_m and K_m are modified Bessel functions of the first and second kinds of m-th order, respectively. The values of the constants A, B, C and F are determined from the boundary conditions of the plate.

Then, the above theory is applied to a circular plate which simulates the thin wheel shown in Fig. 3-2. The boundary conditions are; the inner side (r=a) of the plate is fixed and the outer side (r=b) is free. Therefore, the

deflection and the slope are zero at r=a.

$$w = 0 \tag{3-4}$$

$$\frac{\partial w}{\partial r} = 0 \tag{3-5}$$

The moment and the shear force are zero at r=b.

$$M_r = -D\{\frac{\partial^2 w}{\partial r^2} + \nu(\frac{1}{r}\frac{\partial w}{\partial r} + \frac{1}{r^2}\frac{\partial^2 w}{\partial \theta^2})\} = 0 \tag{3-6}$$

$$V = -D\{\frac{\partial}{\partial r}\nabla^2 w + \frac{1-\nu}{r^2}\frac{\partial^2}{\partial \theta^2}(\frac{\partial w}{\partial r} - \frac{w}{r})\} = 0 \tag{3-7}$$

Substitution of Eq. (3-2) into Eqs. (3-4) to (3-7) gives the following set of four simultaneous, homogeneous equations.

$$AJ_m(ka) + BY_m(ka) + CI_m(ka) + FK_m(ka) = 0 \tag{3-8}$$

$$\begin{aligned} &A\{(m/ka)J_m(ka) - J_{m+1}(ka)\} + B\{(m/ka)Y_m(ka) - Y_{m+1}(ka)\} \\ &+C\{(m/ka)I_m(ka) + I_{m+1}(ka)\} + F\{(m/ka)K_m(ka) - K_{m+1}(ka)\} = 0 \end{aligned} \tag{3-9}$$

$$\begin{aligned} &A[J_m(kb) - \{(1-\nu)/k^2b^2\}\{m(m-1)J_m(kb) + kbJ_{m+1}(kb)\}] \\ &+B[Y_m(kb) - \{(1-\nu)/k^2b^2\}\{m(m-1)Y_m(kb) + kbY_{m+1}(kb)\}] \\ &-C[I_m(kb) + \{(1-\nu)/k^2b^2\}\{m(m-1)I_m(kb) - kbI_{m+1}(kb)\}] \\ &-F[K_m(kb) + \{(1-\nu)/k^2b^2\}\{m(m-1)K_m(kb) + kbK_{m+1}(kb)\}] = 0 \end{aligned} \tag{3-10}$$

$$
\begin{aligned}
&A\,[mJ_m(kb) - kbJ_{m+1}(kb) + \{(1-\nu)/k^2b^2\} \\
&\qquad \times \{m^2(m-1)J_m(kb) - m^2kbJ_{m+1}(kb)\}] \\
&+ B[mY_m(kb) - kbY_{m+1}(kb) + \{(1-\nu)/k^2b^2\} \\
&\qquad \times \{m^2(m-1)Y_m(kb) - m^2kbY_{m+1}(kb)\}] \\
&+ C[mI_m(kb) + kbI_{m+1}(kb) - \{(1-\nu)/k^2b^2\} \\
&\qquad \times \{m^2(m-1)I_m(kb) + m^2kbI_{m+1}(kb)\}] \\
&+ F[mK_m(kb) - kbK_{m+1}(kb) - \{(1-\nu)/k^2b^2\} \\
&\qquad \times \{m^2(m-1)K_m(kb) - m^2kbK_{m+1}(kb)\}] = 0
\end{aligned}
\tag{3-11}
$$

For a non-trivial solution, the characteristic determinant of this set of equations must be zero. This condition leads to the frequency equation, which can be solved by computer methods. Then, introducing the calculated eigenvalues $\lambda_{ms}=k_{ms}b$ (m,s : numbers of nodal diameters and circles) into the system of equations, it is possible to calculate the arbitrary constants A, B, C, and F. Consequently, the dynamic deformation curves and the nodal lines position are obtained.

The vibration of the wheel simply supported at the contacting point with the guide wheel is dealt. In this case, a reactive force P acts on the contact point (r_0,θ_0). The equation of motion becomes

$$D\nabla^4 w - \rho h\omega^2 w = P(r,\theta) \tag{3-12}$$

We assume that w is given in the form of a series of the eigenfunctions w_{ms} as,

$$w = \sum_{ms} C_{ms} w_{ms} e^{i\omega t} \tag{3-13}$$

Since the force P acts only at the contact point, P can be

given by Dirac's delta function as

$$P = P_0\delta(r-r_0)\delta\{r(\theta-\theta_0)\}e^{i\omega t}. \qquad (3\text{-}14)$$

Substituting Eqs. (3-13) and (3-14) into Eq. (3-12), the following equation is obtained.

$$D\nabla^4\Sigma C_{ms}w_{ms} - \rho h\omega^2\Sigma C_{ms}w_{ms} = P_0\delta(r-r_0)\delta\{r(\theta-\theta_0)\} \qquad (3\text{-}15)$$

Since the eigenfunction w_{ms} satisfies Eq. (3-1), we obtain

$$D\nabla^4 w_{ms} - \rho h\omega_{ms}^2 w_{ms} = 0 \qquad (3\text{-}16)$$

where ω_{ms} is the natural angular frequency. Also, the eigenfunctions have the following orthogonality.

$$\int_0^{2\pi}\int_a^b w_{ms}w_{\ell k}rdrd\theta = 0 \quad \text{for } m\neq\ell \text{ or } s\neq k \qquad (3\text{-}17)$$

Substituting Eq. (3-16) into Eq. (3-15), multiplying both sides by w_{ms}, integrating over the surface of the wheel, and with the use of Eq. (3-17), we obtain

$$\rho h(\omega_{ms}^2-\omega^2)C_{ms}\iint w_{ms}^2 rdrd\theta = P_0 w_{ms}(r_0,\theta_0) \qquad (3\text{-}18)$$

The double integration is rewritten as,

$$\int_0^{2\pi}\int_a^b w_{ms}^2 rdrd\theta = \{b^2L(k_{ms}b) - a^2L(k_{ms}a)\}\frac{2\pi}{E_m}$$

where

$$E_m = \begin{cases} 1 & \text{for } m=0 \\ 2 & \text{for } m\geq 1 \end{cases}$$

and

$$\begin{aligned} &L(Z) \\ &=(1/2)\{J_m^2(Z) + J_{m+1}^2(Z) - (2m/Z)J_m(Z)J_{m+1}(Z)\} \\ &+(1/2)\{f_{ms}(Z)\}^2\{Y_m^2(Z) + Y_{m+1}^2(Z) - (2m/Z)Y_m(Z)Y_{m+1}(Z)\} \\ &+(1/2)\{g_{ms}(Z)\}^2\{I_m^2(Z) - I_{m+1}^2(Z) - (2m/Z)I_m(Z)I_{m+1}(Z)\} \end{aligned}$$

$$+(1/2)\{h_{ms}(Z)\}^2\{K_m^2(Z) - K_{m+1}^2(Z) + (2m/Z)K_m(Z)K_{m+1}(Z)\}$$

$$+f_{ms}(Z)[J_m(Z)Y_m(Z) - (m/Z)\{J_m(Z)Y_{m+1}(Z) + J_{m+1}(Z)Y_m(Z)\}$$

$$+J_{m+1}(Z)Y_{m+1}(Z)]$$

$$+(1/Z)g_{ms}(Z)\{J_m(Z)I_{m+1}(Z) + J_{m+1}(Z)I_m(Z)\}$$

$$+(1/Z)h_{ms}(z)\{-J_m(Z)K_{m+1}(Z) + J_{m+1}(Z)K_m(Z)\}$$

$$+(1/Z)f_{ms}(Z)g_{ms}(Z)\{Y_m(Z)I_{m+1}(Z) + Y_{m+1}(Z)I_m(Z)\}$$

$$+g_{ms}(Z)h_{ms}(Z)[I_m(Z)K_m(Z) + (m/Z)\{I_m(Z)K_{m+1}(Z)$$

$$-I_{m+1}(Z)K_m(Z)\} + I_{m+1}(Z)K_{m+1}(Z)]$$

$$+(1/Z)h_{ms}(Z)f_{ms}(Z)\{-Y_m(Z)K_{m+1}(Z) + Y_{m+1}(Z)K_m(Z)\} ,$$

$$f_{ms} = B_{ms}/A_{ms}, \quad g_{ms} = C_{ms}/A_{ms}, \quad h_{ms} = F_{ms}/A_{ms} .$$

From this equation, C_{ms} is obtained. Substituting C_{ms} into Eq. (3-13), the displacement of an arbitrary point is given as,

$$w(r,\theta) = \sum_{ms} \frac{w_{ms}(r,\theta)w_{ms}(r_0,\theta_0)}{\rho h(\omega_{ms}^2-\omega^2)\int\int w_{ms}^2 r dr d\theta} . \qquad (3\text{-}19)$$

Since we assume that the contact point is simply supported, the displacement of the contact point must be zero.

$$w(r_0,\theta_0) = \sum_{ms} \frac{w_{ms}(r_0,\theta_0)^2}{\rho h(\omega_{ms}^2-\omega^2)\int\int w_{ms}^2 r dr d\theta} . \qquad (3\text{-}20)$$

From this equation, the natural angular frequency can be obtained under the condition that the wheel is simply supported at the contact point. Also, the mode of vibration is given by substituting C_{ms} into Eq. (3-20). These modes are referred to as antisymmetric modes.

When the displacement of the eigenfunction at the contact point is zero, the eigenfunction consequently satisfies the supporting condition. Then, the eigenfunctions with $m = \pi/2$ also become the solutions, and these modes are named symmetric modes.

The natural frequencies are given by

$$f = \frac{\omega}{2\pi} = \frac{\lambda^2 h}{2\, b^2}\sqrt{\frac{Eg}{12(1-\nu^2)\gamma}} \quad . \tag{3-21}$$

3.2.2 Result of numerical calculations

The numerical calculation is carried out with the following figures.

inner radius (a) : 25.0 mm, outer radius (b) : 5 mm,
E : 2.1×10^4 kgf/mm^2, ρ : 7.86×10^{-10} kgf sec^2/mm^4,
ν : 0.3.

The calculated eigenvalues λ_{ms}'s are shown in Table 3-1. These eigenvalues also become the eigenvalues of the symmetric modes. Then, substituting these eigenfunctions into Eq. (3-20), the eigenvalues of antisymmetric modes λ's are calculated. The mode shapes with contour lines of $\lambda = 2.833$ and $\lambda = 3.442$ are shown in Fig. 3-3. These results will be compared with the experimental ones later. The eigenvalues, natural frequencies and the symmetric and the antisymmetric modes are shown in Fig. 3-4.

3.2.3 Experimental apparatus

The experimental apparatus shown in Fig. 3-5 is composed of a press device, a test wheel, a guide wheel which simulates a rail, and a motor. The press device gives the

necessary load to the test wheel by a coil spring, and the load is measured by strain gauges attached to a plate located between the coil spring and the test wheel. The test wheel which is used in this section is shown in Fig. 3-1. The outer diameter of the guide wheel is 300 mm and its thickness is 30 mm, The test thin wheel and the guide wheel is made of S55C steel. Both of the wheels are supported by plane bearings with forced lubrication. The guide wheel is connected to the 1 HP motor by a plane belt. The bed of the motor is separated from the bed of the wheels in order to cut off vibration. The motor is covered with a sound-proof box. The measurement system of the vibration and the sound is shown in Fig. 3-6. The vibrational acceleration is measured by a piezoelectric accelerometer (Bruel and Kjær 4344). The sound pressure is measured by a condensor microphone (Bruel and Kjær 4131). Both detectors' frequency characteristics are linear up to 20 kHz. The spectrum is obtained by an FFT analyzer (Nicolet 440A).

3.2.4 Experimental procedure

Non-running experiment

First, the test wheel is set to contact with the guide wheel with a load 50-150 kgf. White noise vibration is given to the axial center of the thin wheel, and the acceleration is measured by the accelerometer which is attached to the rim. The frequency spectrum is investigated by the FFT analyzer. Then, the thin wheel is separated from the guide wheel, and the same experiment is carried out. In the contact condition, the test wheel is

excited by a harmonic force whose frequency is the same as that of the peaks of the spectrum, and the mode shapes are investigated by checking the phase angle of each point. Also, Chladni's pictures of the mode shapes are obtained. Furthermore, the vibrational characteristics of the guide wheel are investigated.

Running experiment

The acceleration and noise of the running thin wheel are investigated. The rotational speed is varied from 400 to 1500 rpm. The electric signal of the measured acceleration is transmitted through a slipring. The microphone is located near the thin wheel. The rotational speed is measured photoelectrically. The vibration of the bed is also investigated.

3.2.5 Results of experiments

Non-running experiment

Figure 3-7 shows the acceleration spectra of the thin wheel under the white noise excitation. The upper spectrum of this figure is the result with the load, and the lower one is without the load. The resolving power in the frequency range of 0-10 kHz is 25 Hz. The upper spectrum has large peaks at 1000-1750, 1900, 2625, 3125, 4200, 5100, 6300, 7575, and 8300 Hz. The lower spectrum has large peaks at 1400, 1900, 3125, 5100, and 7575 Hz. The amplitudes of the peaks vary according to the position of the accelerometer; the nearer the accelerometer is to the nodal line, the smaller the amplitudes are.

The mode shapes for each of the resonant frequencies 1750, 1900, 2625, 3175, 4200, 5100, 6300, 7500, and 8300 Hz coincide with the calculated ones shown in Fig. 3-4. The Chladni's pictures of the resonant frequencies 1750 and 2625 Hz are shown in Fig. 3-8. They agree well with the theoretical predictions shown in Fig. 3-3.

The resonant frequencies of the guide wheel are 1825, 2250, 3725, 4700, 6050, 6900, and 9125 Hz.

Rolling experiment

Figure 3-9 shows the spectra of the vibrational acceleration and the sound pressure of the rolling thin wheel. Both spectra are in a good agreement, and they have peaks at 1400, 1750, 2600, 3125, 4250, 6300, 7500, and 8300 Hz. From this, we can see that the noise is dominated by the transverse vibration of the thin wheel. The high peak of the sound pressure in the frequency range below 1000 Hz is due to the vibration of the bed whose spectrum is shown in Figure 3-10.

The frequency characteristics of vibrational acceleration of the rolling and the non-rolling experiments are similar. The peaks at 3725 and 6050 Hz of the rolling experiment are due to the vibration of the guide wheel. The vibration of the guide wheel slightly influences the vibration of the thin wheel. Table 3-2 shows a comparison between the theoretical and the experimental results. From this table, we can see that all results agree well, and the theoretical analysis, especially that of the antisymmetric modes which is obtained under the assumption that the wheel is simply supported at the contact point, is confirmed.

3.3 Vibration of a Web Wheel

3.3.1 Theoretical analysis

The vibration of the web wheel is analyzed by Mindlin theory[5,6] which includes the effects of the shear deformation and the rotatory inertia. First, the basic equations are explained. The assumptions for displacements (u_r, u_θ, u_z) are

$$U_r = z\psi_r(r,\theta,t), \tag{3-22}$$

$$U_\theta = z\psi_\theta(r,\theta,t), \tag{3-23}$$

$$U_z = w(r,\theta,t). \tag{3-24}$$

In this case, the moments M_r, M_θ, M_r and shear forces Q_r, Q_θ are given by the following equations.

$$M_r = D\{\frac{\partial\psi_r}{\partial r} + \frac{\nu}{r}(\psi_r + \frac{\partial\psi_\theta}{\partial\theta})\}, \tag{3-25}$$

$$M_\theta = D\{\frac{1}{r}(\psi_r + \frac{\partial\psi_\theta}{\partial\theta}) + \nu\frac{\partial\psi_r}{\partial r}\}, \tag{3-26}$$

$$M_{r\theta} = \frac{D}{2}(1-\nu)\{\frac{1}{r}(\frac{\partial\psi_r}{\partial\theta} - \psi_\theta) + \frac{\partial\psi_\theta}{\partial\theta}\}, \tag{3-27}$$

$$Q_r = G'h(\psi_r + \frac{\partial w}{\partial r}), \tag{3-28}$$

$$Q_\theta = G'h(\psi_\theta + \frac{1}{r}\frac{\partial w}{\partial\theta}), \tag{3-29}$$

where, $G'=\pi^2/12G$ (G:shear modulus).

The equations of motion for ψ_r, ψ_θ, and w are

$$\frac{\partial M_r}{\partial r} + \frac{1}{r}\frac{\partial M_{r\theta}}{\partial \theta} + \frac{M_r - M_\theta}{r} - Q_r = \frac{\rho h^3}{12}\frac{\partial^2 \psi_r}{\partial t^2}, \tag{3-30}$$

$$\frac{\partial M_{r\theta}}{\partial r} + \frac{1}{r}\frac{\partial M_\theta}{\partial \theta} + \frac{2M_{r\theta}}{r} - Q_\theta = \frac{\rho h^3}{12}\frac{\partial^2 \psi_\theta}{\partial t^2}, \tag{3-31}$$

$$\frac{\partial Q_r}{\partial r} + \frac{1}{r}\frac{\partial Q_\theta}{\partial \theta} + \frac{Q_r}{r} + P = \rho h \frac{\partial^2 w}{\partial t^2}. \tag{3-32}$$

Two of the plate displacement components ψ_r and ψ_θ are assumed to be expressed in terms of the potentials ϕ and H which give rise to the areal dilatation and rotation as,

$$\phi_r = \frac{\partial \phi}{\partial r} + \frac{1}{r}\frac{\partial H}{\partial \theta}, \tag{3-33}$$

$$\psi_\theta = \frac{1}{r}\frac{\partial \phi}{\partial \theta} - \frac{\partial H}{\partial r}. \tag{3-34}$$

When the external force P is negligible, the potential ϕ is assumed to be $(\sigma-1)w$, and the following equations are obtained.

$$w = w_1 + w_2, \tag{3-35}$$

$$\psi_r = (\sigma_1 - 1)\frac{\partial \omega_1}{\partial r} + (\sigma_2 - 1)\frac{\partial \omega_2}{\partial r} + \frac{1}{r}\frac{\partial H}{\partial \theta}, \tag{3-36}$$

$$\psi_\theta = (\sigma_1 - 1)\frac{1}{r}\frac{\partial \omega_1}{\partial \theta} + (\sigma_2 - 1)\frac{1}{r}\frac{\partial \omega_2}{\partial \theta} - \frac{\partial H}{\partial r}, \tag{3-37}$$

$$(\nabla^2 + \delta_1^2)w_1 = 0, \tag{3-38}$$

$$(\nabla^2 + \delta_2^2)w_2 = 0, \tag{3-39}$$

$$(\nabla^2 + \delta_3^2)H = 0, \tag{3-40}$$

$$\delta_1^2, \delta_2^2 = \frac{1}{2}\delta_0^4[R+S\pm\{(R-S)^2+4\delta_0^{-4}\}^{1/2}] ,$$

$$\sigma_1, \sigma_2 = (\delta_2^2, \delta_1^2)(R\delta_0^4 - S^{-1})^{-1} ,$$

$$\delta_3^2 = 2(R\delta_0^4 - S^{-1})/(1-\nu),$$

$$R = \frac{h^2}{12} , \quad S = \frac{D}{G'h} , \quad \delta_0^4 = \frac{\rho\omega^2 h}{D} .$$

The solution of Eqs. (3-38) to (3-40) are

$$w_1 = \{A_{11}J_m(\delta_1 r) + A_{12}Y_m(\delta_1 r)\}\cos m\theta , \qquad (3\text{-}41)$$

$$w_2 = \{A_{21}J_m(\delta_2 r) + A_{22}Y_m(\delta_2 r)\}\cos m\theta , \qquad (3\text{-}42)$$

$$H = \{A_{31}J_m(\delta_3 r) + A_{32}Y(\delta_3 r)\}\sin m\theta . \qquad (3\text{-}43)$$

When δ_2^2 and δ_3^2 are negative, J_m and Y_m are replaced by modified Bessel function I_m and K_m, respectively. By setting R=S=0, δ_1^2, δ_2^2 become δ_0^2, and the above equations are reduced to those of the thin plate theory which neglects the effects of shear deformation and rotatory inertia.

In the next step, we derive the vibration of the web wheel shown in Fig. 3-11. The basic equations explained above are applied to the web and the rim independently. As the boundary conditions we assume that the inner side of the web is fixed, the outer side of the rim is free, and the outer side of the web and the inner side of the rim are continuous. In the following equations, suffix W and R represent the web and the rim, respectively.

The displacement and slopes are zero at r=a.

$$w^W_{r=a} = 0 , \qquad (3\text{-}44)$$

$$\psi^{W}_{r,r=a} = 0 \quad , \tag{3-45}$$

$$\psi^{W}_{\theta,r=a} = 0 \quad . \tag{3-46}$$

The moments and the shear force are zero at r=b.

$$M^{R}_{r,r=c} = 0 \quad , \tag{3-47}$$

$$M^{R}_{r\theta,r=c} = 0 \quad , \tag{3-48}$$

$$Q^{R}_{r,r=c} = 0 \quad . \tag{3-49}$$

The following equations are derived from the condition of continuity at r=b.

$$w^{W}_{r,r=b} = w^{R}_{r=b} \quad , \tag{3-50}$$

$$\psi^{W}_{r,r=b} = \psi^{R}_{r,r=b} \quad , \tag{3-51}$$

$$\psi^{W}_{\theta,r=b} = \psi^{R}_{\theta,r=b} \quad , \tag{3-52}$$

$$M^{W}_{r,r=b} = M^{R}_{r,r=b} \quad , \tag{3-53}$$

$$M^{W}_{r\theta,r=b} = M^{R}_{r\theta,r=b} \quad , \tag{3-54}$$

$$Q^{W}_{r,r=b} = Q^{R}_{r,r=b} \quad . \tag{3-55}$$

Substituting Eqs. (3-41) to (3-43) for the web and the rim into Eqs. (3-44) to (3-55), simultanuous homogeneous equations with the unknowns A^{i}_{jk} (i=W,R, j=1,2,3, and k=1,2) can be obtained. Elimination of the determinant of these coefficients yields an equation for the determination of the natural frequency. Then, by solving the simultaneous equations, the mode shapes can be obtained.

3.3.2 Results of numerical calculations

The calculated natural frequencies of the web wheel are shown in Table 3-3. In order to investigate the effects of the shear deformation and the rotatory inertia, the natural frequencies obtained by the thin plate theory, which was mentioned in section 3.2 are also shown in the same table. Since the natural frequencies are inversely proportional to the size of the wheel, the natural frequencies of the actual wheel are 1/6 of those of the test wheel.

The displacement curves of the mode shapes of the web wheel in the circumferential direction are constant for m=0, and sine curves for m are greater than 0. The displacement curves in the radial direction are shown in Fig. 3-12 by solid lines. The curves for a circular plate which has a uniform thickness of 5 mm are also shown by dotted lines in the same figure.

3.3.3 Experimental results

The vibration and the noise of the web wheel are measured. The experimental procedure is similar to the one used for the thin wheel mentioned in the previous section.

Rolling experiment

The frequency spectra of the sound pressure and the vibrational acceleration in the axial direction of the web wheel which is rolling with a 50 kgf load and a 1000 rpm rotational speed are shown in Fig. 3-13. The vibration of the rim has the same frequency spectrum as the web. The

vibrational amplitudes of the web and the rim are in good agreement with the theoretical results shown in Fig. 3-12. When the load and the rotational speed are varied, the frequencies corresponding to the peaks are constant.

Non-rolling experiment

Impulse response of vibration of the web wheel which is separated from the guide wheel is shown in the bottom row of Fig. 3-13. The mode shapes and displacement curves are in good agreement with the theoretical predictions shown in Fig. 3-13 and Fig. 3-12.

3.3.4 Discussions on results

In the theoretical analysis, the vibration of normal mode of the web wheel is obtained under the boundary condition that the whole outer circumference is free. Therefore, the natural frequencies obtained here correspond to the symmetric modes. However, since the wheel contacts with a rail, the antisymmetric modes due to this contact condition should be taken into consideration. In the case of the experimental apparatus, the spectrum of the rolling vibration shown in Fig. 3-13 has small peaks at 9500 and 15000 Hz. These peaks seem to be due to the antisymmetric modes. However, the antisymmetric modes are not discussed in this chapter because the coupled vibration of the wheel and the rail will be studied in chapter 6.

As noted before, the wheel's thickness is considerably large compared with its diameter. Therefore, in the theoretical analysis, the effects of shear deformation and rotatory inertia are taken into consideration. As shown in

Table 3-3, the natural frequencies obtained by the thick and the thin plate theories are almost identical in the low order modes. However, the latter is considerably higher than the former in the high order modes. For example, the natural frequencies of (5,0) mode are 17014 Hz (thick plate theory) and 22564 Hz (thin plate theory), and its rate of increase is 32%. The web wheel which is used in this experiment does not have many high order modes in the audio frequency range, 20-20000 Hz. However, the wheel with the actual size has many high order modes in the audio frequency range, and so they should be obtained by the thick plate theory.

Comparing the displacement curves of the web wheel with the circular plate with a uniform thickness of 5 mm in Fig. 3-13, there is little difference between them for the modes with s=0. For the modes with s which is greater than 0, the amplitude of reflection at the rim is small, and the nodal circle shifts to outer portion. These tendencies become more apparent when the thickness of the rim increases.

3.4 Conclusions

In this chapter, the transverse vibrations of the thin wheel and the web wheel are analyzed theoretically. Also, the vibration and the noise are experimentally investigated. Then, the following conclusions are obtained.

i) The noise is dominated by the transverse vibration of the wheel.

ii) The vibrations of the thin wheel and the web wheel can be theoretically analyzed by the thin plate theory and

Mindlin theory, respectively.

iii) The frequency spectra of the vibration of the rolling wheels are similar to those of the non-rolling wheels.

iv) The vibrations of the wheels have symmetric and antisymmetric modes, and the antisymmetric modes clearly appear in the vibration of the thin wheel under high load.

REFERENCES

1) Susumu,S., & Matsuhisa,H., Bull.JSME, 21-160 (1978), 1475.

2) Matsuhisa,H., et al., Bull.JSME, 24-191 (1981), 849.

3) Irie,T., & Yamada,G., Trans.JSME, 44-379 (1978), 895.

4) Nakazawa,A., Trans.JSME, 33-256 (1967), 1951.

5) Mindlin,R.D., J.Appl.Mech., 18 (1951), 31.

6) Mindlin,R.D., & Deresiewicz,H., J.Appl.Phys., 25-10 (1954), 1329.

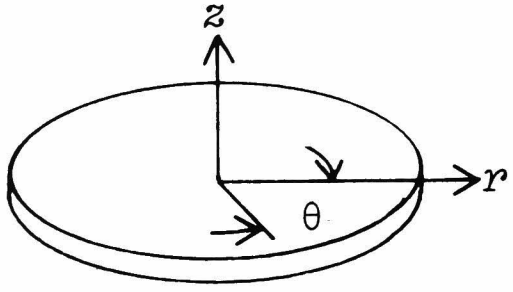

Fig. 3-1 Cylindrical coordinates.

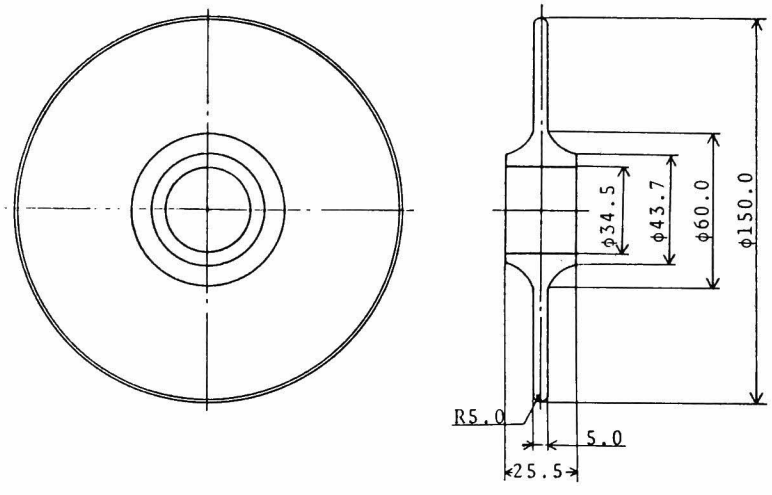

Fig. 3-2 Shape of the thin wheel.

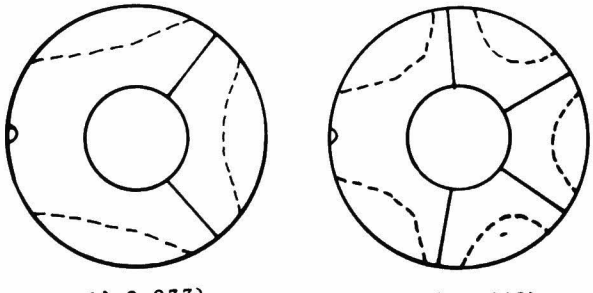

Fig. 3-3 Mode shapes of the thin wheel.

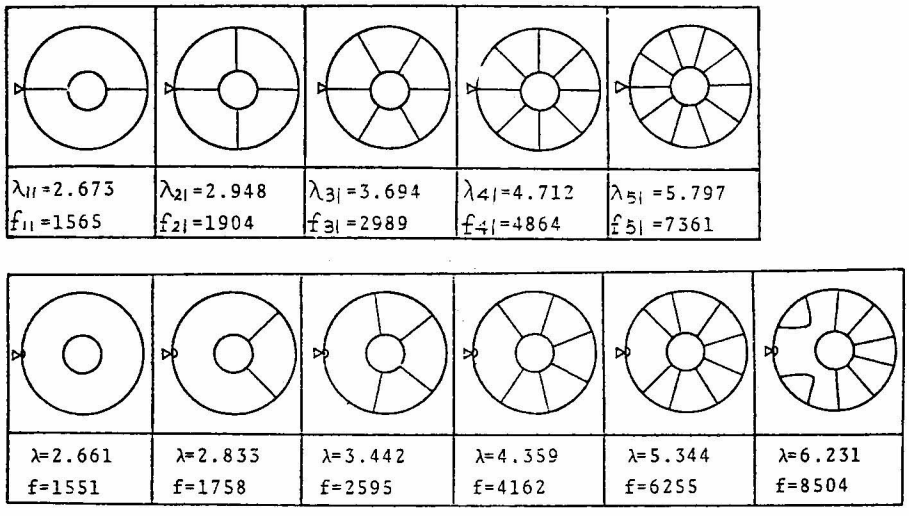

Fig. 3-4 Mode shapes, eigenvalues, and natural frequencies of the thin wheel; upper low : symmetric modes, lower row : antisymmetric modes.

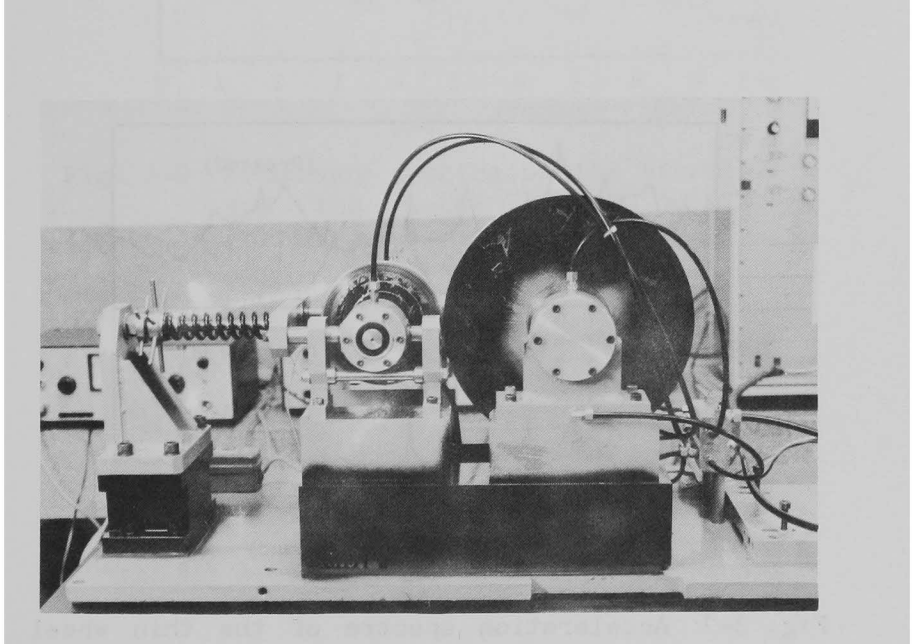

Fig. 3-5 Experimental apparatus.

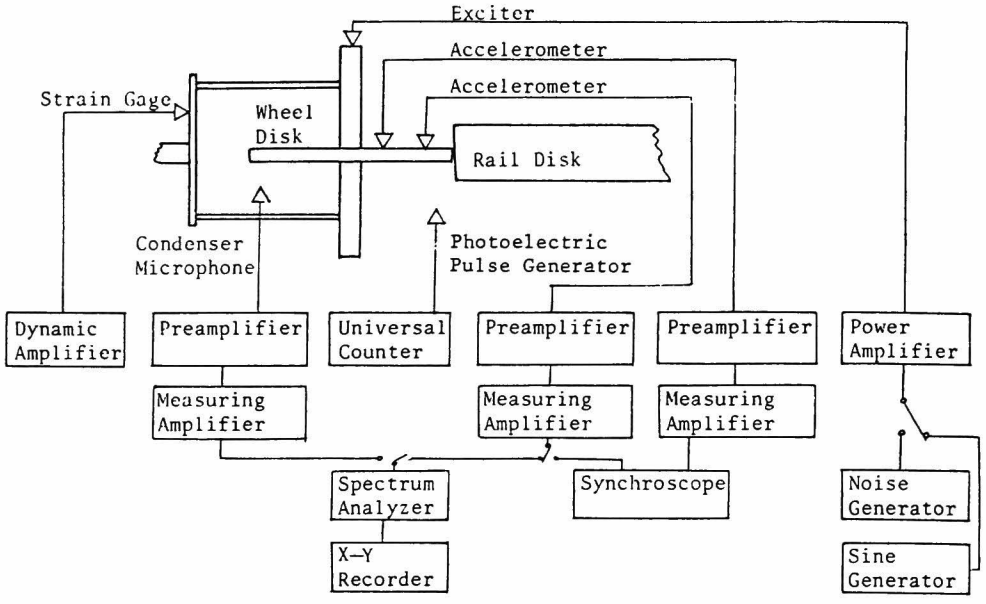

Fig. 3-6 Block diagram of measurement.

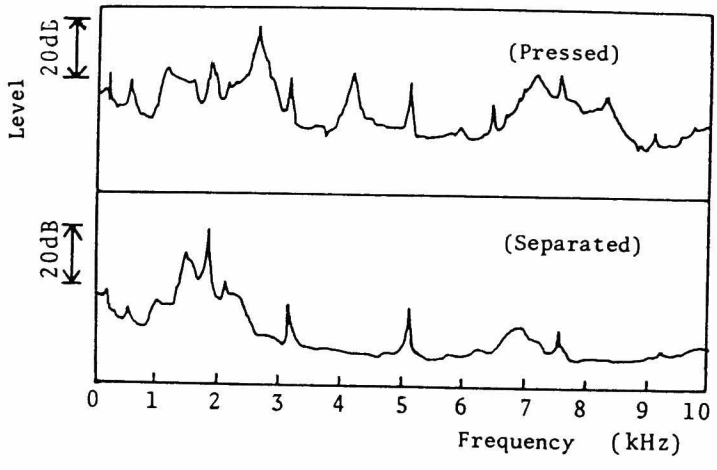

Fig. 3-7 Acceleration spectra of the thin wheel under the white noise excitation.

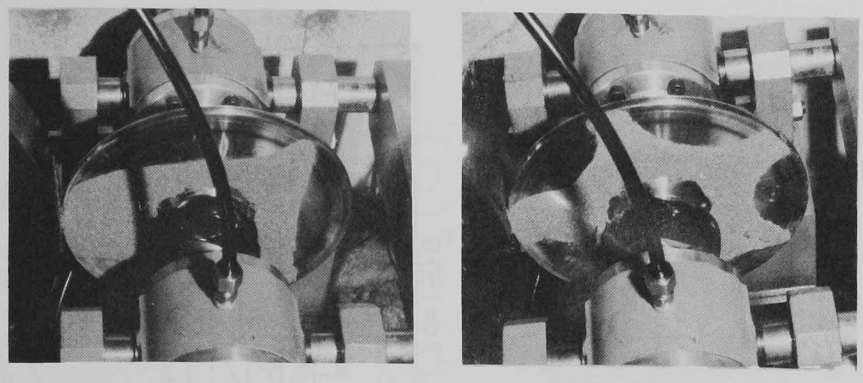

Fig. 3-8 Chladni's pictures of the antisymmetric modes.

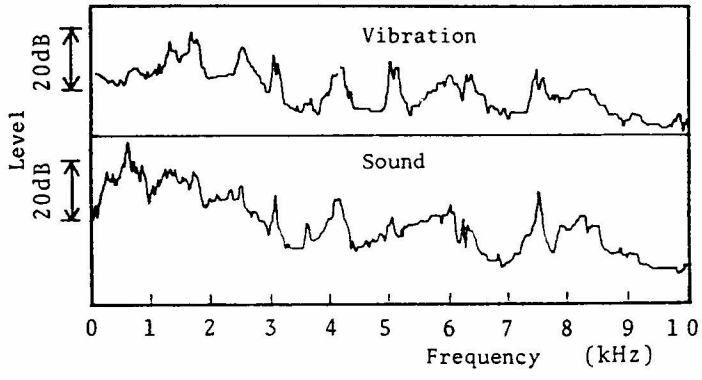

Fig. 3-9 Frequency spectra of the vibration and the noise caused by the rolling thin wheel.

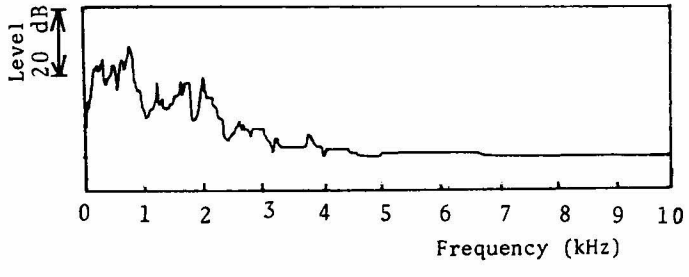

Fig. 3-10 Frequency spectrum of the bed's vibration.

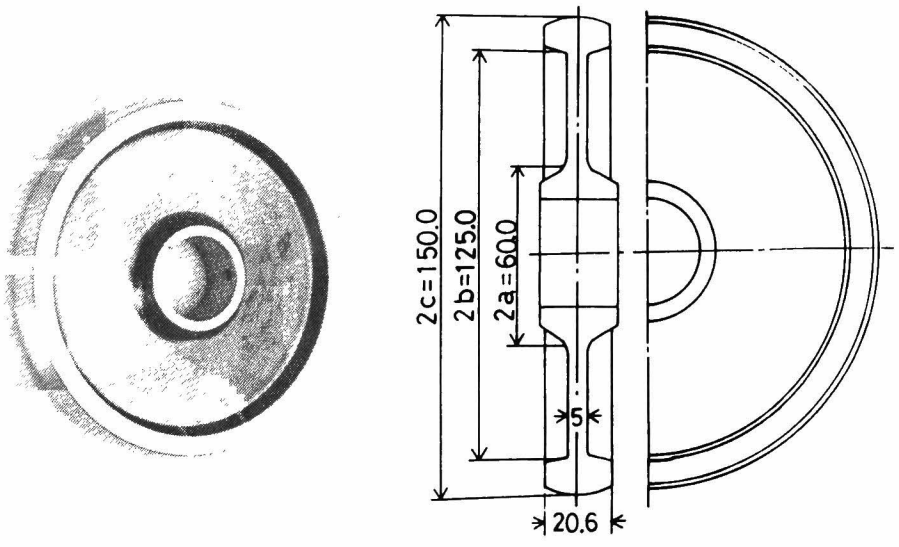

Fig. 3-11 Shapes of the web wheel.

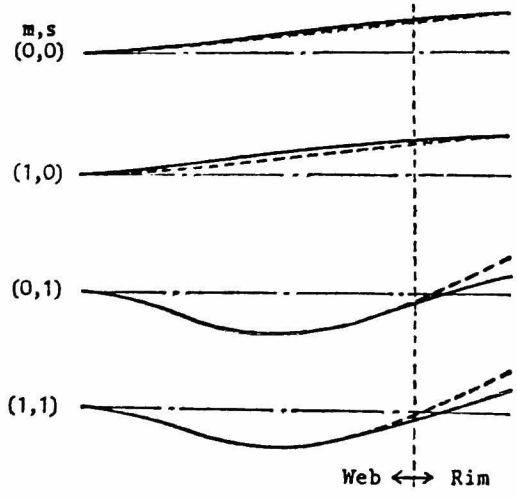

Fig. 3-12 Displacement curves in the radial direction of the web wheel.

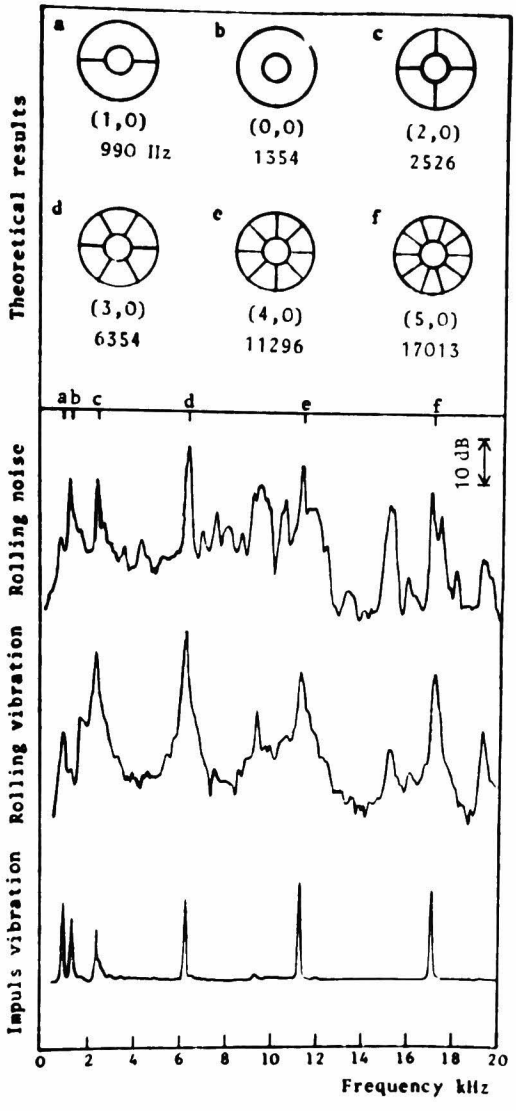

Fig. 3-13 Frequency spectra of the vibration and the noise caused by the rolling web wheel.

Table 3-1 Calculated eigenvalues of the thin wheel.

s	m=0	m=1	m=2	m=3	m=4	m=5	m=6	m=7	m=8
1	2.655	2.673	2.948	3.694	4.712	5.797	6.886	7.966	9.040
2	6.727	6.872	7.305	8.006	8.923	9.987	11.130	12.307	13.490
3	11.443	11.542	11.841	12.340	13.030	13.891	14.891	15.994	17.161

Table 3-2 Calculated natural frequencies of the web wheel.

s \ m	0	1	2	3	4	5	6	7
1	1349	954	2305	6208	11300	17114	23378	29922
	1376	1019	2854	7524	14170	22564	32140	41727
2	9140	9926	12084	15198	19164	23378	29448	35540
	11252	13710	16898	20175	24542	30456	38408	49413

(Hz)

Table 3-3 Measured and calculated natural frequencies of the thin wheel.

Mode									
Theoretical calculation	1758	1904	2595	2989	4162	4864	6255	7361	8504
Rolling ex.	1750	1900	2600	3125	4275	5050	6300	7500	8300
Non-rolling pressed ex.	1750	1900	2625	3175	4200	5100	6300	7575	8300
Non-rolling separated ex.	—	1900	—	3175	—	5100	—	7575	—

(Hz)

CHAPTER 4 EFFECTS OF VELOCITY, LOAD AND CONTACT ANGLE

4.1 Introduction

In chapter 2, the relation between the noise and the train velocity of the Shinkansen was discussed. In this chapter, the effects of the velocity and load on the noise and vibration are investigated by making use of the experimental apparatus[1)]. When a train is traversing on a curve, large noise is generated. In this study, the curve is simulated by a contact angle between the wheel and rail. The effect of the contact angle on the vibration and noise is also experimentally investigated.

4.2 Experimental Results

4.2.1 Web wheel

Figure 4-1 shows the schematic diagram of the contact angle between the wheel and the guide wheel, which simulates the situation of a train traversing on a curve. Figure 4-2 shows the relations betweeen the rotational speed and the total levels of the vibrational acceleration and the sound pressure for several contact angles, in which the load is 30 kgf. When the rotational speed is doubled, the acceleration level increases by about 8 dB and the sound pressure level by about 3 to 4 dB. Both levels increase significantly as the contact angle increases. However, the load hardly has an influence on both levels.

Figure 4-3 shows the frequency specra of the acceleration and the sound pressure for $\alpha=0$ and $\alpha=0.01$. As shown

in this figure, the peaks at the natural frequencies become higher and sharper with the increase of the contact angle. When the rotational speed increases, the levels of the peaks increase, however the shapes of the spectra are almost the same. The influence of the load on the levels and spectra of both vibration and the noise is negligible.

4.2.2 Thin wheel

Figure 4-4 shows the wave forms of the vibrational acceleration and the sound pressure for $\alpha = 0$. When the rotational speed increases the amplitudes of the vibration and the noise increase. The large amplitude oscillations appear at the large corrugations. The intervals between these oscillation become shorter with the increase of the rotational speed. When the contact angle increases, the amplitudes become larger. The web wheel has the same tendency as the thin wheel.

Figure 4-5 shows the spectra of vibrational acceleration of the thin wheel for several rotational speeds and loads. When the load is 120 kgf, all peaks increase with the rotational speed, but when the load is 30 kgf, the peaks of the symmetric modes (3125, 5050, 7500 Hz, etc.) increase more than those of the antisymmetric modes as shown in Fig. 4-6.

In Fig. 4-5, the peaks for high rotational speed are divided into two. The modes of vibration are formed on the disk. However, they are immediately attenuated, and new modes whose nodal lines pass through the contact point are formed because the propagation velocity of flexural vibration which generates the modes is high enough. Therefore,

the modes are considered to be stationary in space, and the deflection w of a symmetric mode is given as,

$$w = A(r)\sin(m\omega_z t)\cos(\omega t),$$

where, A(r) : the maximum amplitude at radius r,

m : the number of diametric nodal lines,

ω_z : the angular frequency of rotation ($120\pi n$),

n : rate of rotation of the wheel (rpm),

ω : the natural frequency.

This equation is rewritten as,

$$w = 1/2\ \{A(r)\ \sin(\omega+m\omega_z)t + \sin(\omega-m\omega_z)t\}.$$

The angular frequency is divided into $(\omega+m\omega_z)$ and $(\omega-m\omega_z)$. When $m\omega_z$ is small compared with ω, there is little difference between $(\omega+m\omega_z)$ and $(\omega-m\omega_z)$. When the rotational speed and the number of diametric nodal lines are large, the spectra have peak splits. For example, when m=4 and n=600, 1000 and 1400 rpm, the distance of the peak splits are 80, 133 and 186 Hz, respectively. The peaks of the antisymmetric modes are not so sharp as those of the symmetric modes, because they are given by the sum of symmetric modes.

In case of the thin wheel, the antisymmetric modes and the peak splits clearly appear, while in case of the web wheel, they do not. Since the wheel is thin enough compared with the guide wheel, the boundary condition at the contact point is assumed to be simply supported. However in the case of the web wheel which is considerably thicker, this assumption can not be adopted.

4.3 Conclusions

In this chapter, the effects of the rotational speed, the load, and the contact angle on the vibration and the noise are investigated experimentally. Then, the following conclusions are obtained.

i) The vibration is dominated by the corrugation and the roughness of the contact surface of the wheels.

ii) When the rotational speed of the web wheel is doubled, the total level of the vibrational acceleration increases by about 8 dB, and that of the sound pressure by 3 to 4 dB. However, the load does not influence on the total levels. The spectra of the vibration and the noise are not influenced by the rotational speed and the load.

iii) The vibration and the noise increase remarkably with the contact angle.

iv) When the wheel is considerably thinner than the guide wheel, the antisymmetric modes become significant under the high load.

REFERENCE

1) Matsuhisa,H., & Sato,S., Bull.JSME, 22-173 (1979), 1626.

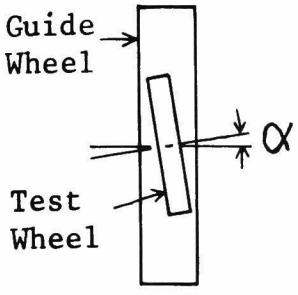

Fig. 4-1 Contact angle.

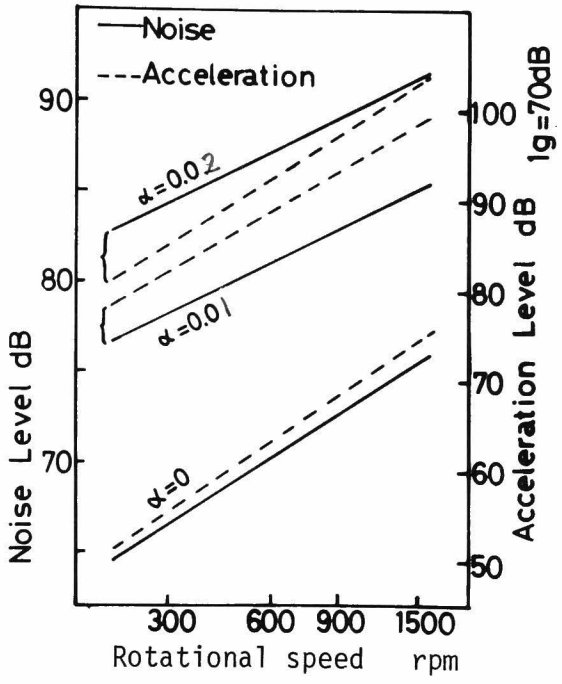

Fig. 4-2 Relation between the acceleration level and the rotational speed of the web wheel.

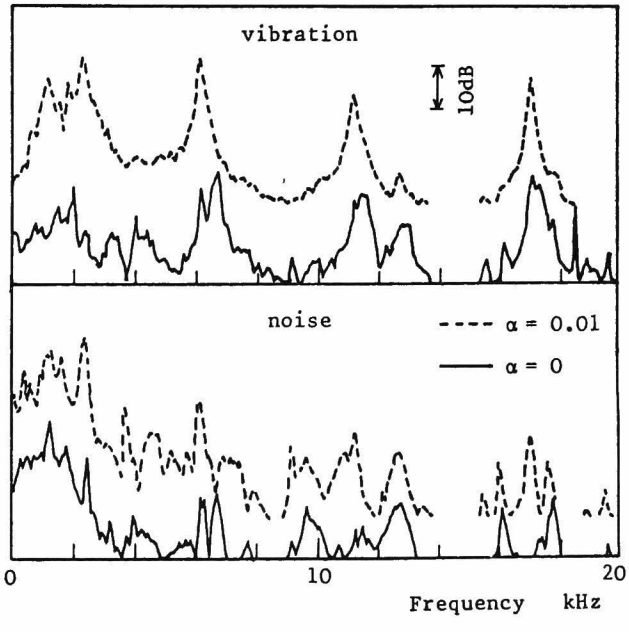

Fig. 4-3 Frequency spectra of the acceleration and the sound pressure of the web wheel.

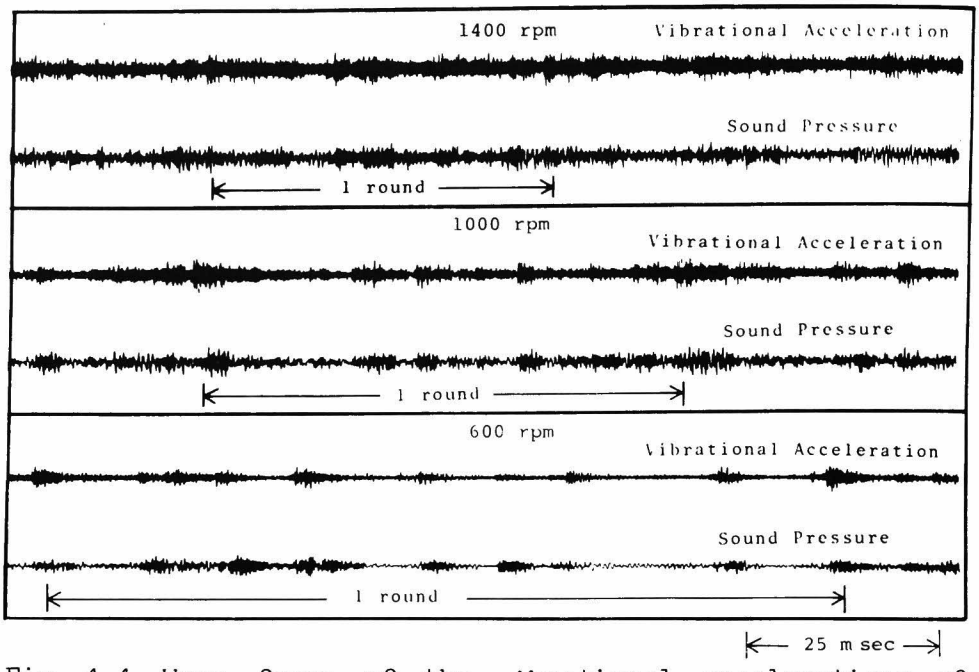

Fig. 4-4 Wave forms of the vibrational accelerations of the thin wheel for several rotational speed and the load.

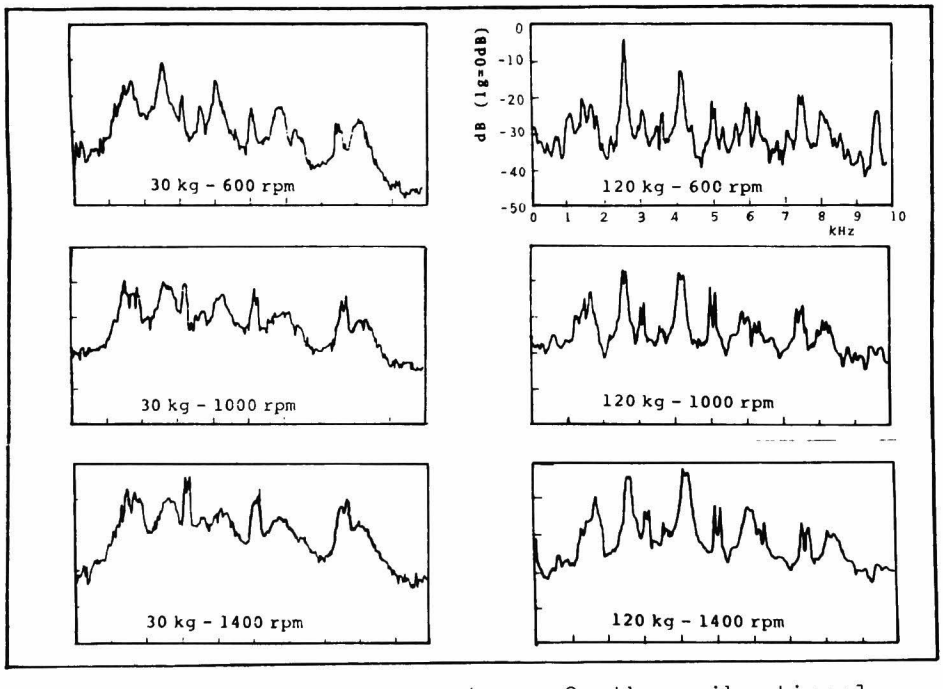

Fig. 4-5 Frequency spectra of the vibrational acceleration of the thin wheel for several rotational speeds and the loads.

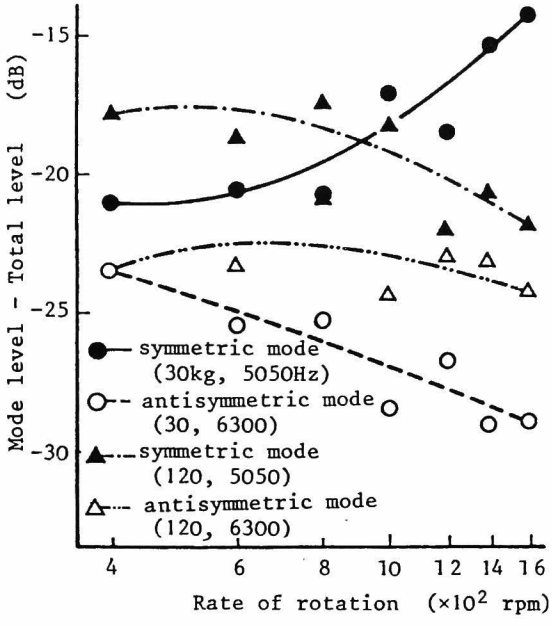

Fig. 4-6 Ratio of acceleration level of each mode to total acceleration level.

CHAPTER 5 ACOUSTIC RADIATION

5.1 Introduction

The relation between the sound and the vibration is important in the study of the noise generated by the train's wheel. In this chapter, acoustic radiation coefficient $\bar{W}/\bar{H}$ is introduced[1], in which $\bar{W}$ is the radiated acoustic power[2] and $\bar{H}$ is the mechanical power of the vibrating wheel. The characteristics of the noise are theoretically investigated by means of the acoustic radiation coefficient of the normal modes. Furthermore, the theoretical calculation for the thin wheel and the web wheel is carried out. These results are compared with the experimental results.

5.2 Theoretical Analysis

Figure 5-1 shows the polar coordinates for this analysis. On the assumption that point B on the disk is a sound source, the velocity potential at A on the disk due to a small elementary area dB, distant R from B, is

$$d\phi = i \frac{\omega w(r_2,\theta_2)dB}{2\pi R} e^{i(\omega t-kR)} , \qquad (5\text{-}1)$$

$$R = \sqrt{r_1^2+r_2^2-2r_1r_2\cos(\theta_2-\theta_1)} ,$$

where ω:angular frequency,

w:amplitude of displacement,

k:wave number (ω/c),

c:sound velocity.

The total sound pressure at A will be obtained by integrating the contributions from the whole surface of the disk and so,

$$\phi = \int_0^{2\pi}\int_a^b i \frac{\omega w(r_2,\theta_2)}{2\pi R} e^{i(\omega t-kR)} r_2 dr_2 d\theta_2 . \qquad (5\text{-}2)$$

Also, the sound pressure generated from the back side of the disk has an effect on the velocity potential at A, but it is diffracted by 180 degrees, therefore, the velocity potential from the reverse side is negligible. The sound pressure at A is given by

$$P = \rho' \frac{\partial \phi}{\partial t} = -\rho'\omega^2 \frac{e^{i\omega t}}{2\pi} \int_0^{2\pi}\int_a^b \frac{\omega(r_2-\theta_2)}{R} e^{-ikR} r_2 dr_2 d\theta_2, \qquad (5\text{-}3)$$

where ρ' is the equivalent density of the transmitting medium. The particle velocity v at the surface is equal to the vibration velocity of the disk.

$$v = i\omega w(r_1,\theta_1)e^{i\omega t} . \qquad (5\text{-}4)$$

The acoustic power dW of the elementary area dA at the point A is

$$dW = R_e(p)R_e(v)dA$$

$$= \frac{\rho'\omega^3 w(r_1,\theta_1)}{2\pi} \int_0^{2\pi}\int_a^b \frac{\omega(r_2,\theta_2)}{R} \{\sin(\omega t)\cos(\omega t)$$

$$\cos(-kR)-\sin^2(\omega t)\sin(-kR)\} r_2 dr_2 d\theta_2 dA . \qquad (5\text{-}5)$$

The total acoustic power $\bar{W}$ can be obtained by integrating dW with respect to dA and making a time average, and

multiplying by two (the reverse side has the same power).

$$\bar{W} = \frac{\rho'\omega^3}{2\pi} \int_0^{2\pi}\int_a^b \{\omega(r_1,\theta_1)\int_0^{2\pi}\int_a^b \frac{\omega(r_2,\theta_2)}{R} \sin(kR) r_2 dr_2 d\theta_2\} r_1 dr_1 d\theta_1 \quad . \tag{5-6}$$

On the other hand, the mechanical power of the vibrating elementary area dA is

$$d\bar{H} = \frac{\gamma h}{g} \omega \bar{v}^2 dA \quad , \tag{5-7}$$

where

$$\bar{v}^2 = \frac{1}{2} \omega^2 w^2(r_1,\theta_1) \quad ,$$

and, γ:specific weight of the plate, h:thickness of the plate. Integrating dH with respect to dA, the mechanical power $\bar{H}$ is

$$\bar{H} = \frac{\gamma h \omega^3}{2g} \int_0^{2\pi}\int_a^b \omega^2(r_1,\theta_1) r_1 dr_1 d\theta_1 \quad . \tag{5-8}$$

5.3 Numerical Calculations and Discussions

The numerical calculation of the coefficient $\bar{W}/\bar{H}$ for three kind of thin disks with an uniform thickness is carried out. One of the disks has 50 mm inner diameter and 150 mm outer diameter which is used in the previous chapters, another has 100 mm inner and 300 mm outer diameters, and the third has 150 mm inner, 450 mm outer diameters, and all are of 5 mm thickness. The boundary conditions are that the inner circumference is fixed, the outer is free,

and one point on the outer circumference is simply supported. The results are shown in Figs. 5-2, 5-3, and 5-4, in which f_c is the coincidence frequency where the velocity of the sound wave in air and that of the bending wave of the plate are equal as,

$$f_c = \frac{c^2}{2\pi}\sqrt{\frac{M}{B}} \quad , \tag{5-9}$$

where, $B=EI/(1-\nu^2)$, $M=\rho h$, $I=h^3/12$.

The coincidence frequency of the steel plate with a thickness of 5 mm is 2377 Hz. When the number of diametric nodal lines m is 0 or 1, $\bar{W}/\bar{H}$ has a large value, and with an increase of frequency, $\bar{W}/\bar{H}$ decreases rapidly, then increases again to a peak value, and finally monotonically decreases. The disk with 150 mm outer diameter has a peak at $f \cong 2f_c$. Comparing these three figures, we see that as the diameter increases, the frequency of the peak approaches f_c and the value of the peak becomes larger. In Gösele's coefficient[3], when the plate is infinite, the radiation coefficient is 0 at $f<f_c$, infinite at $f=f_c$, and then monotonically decreases to 1 at $f>f_c$. However, the disks have finite largeness, so the peaks are not infinite, and $\bar{W}/\bar{H}$ is not 0 at $f<f_c$. When the size of the disk increases, the frequency of the peak comes close to f_c and $\bar{W}/\bar{H}$ has very small value at $f<f_c$ for the low order resonant vibrations.

Figure 5-5 shows the experimentally measured frequency spectra of the vibrational accelerations and the sound pressures of the thin wheel disk. The rate of rotation is 1000 rpm and the loads are 30 and 120 kgf. In a comparison between the values of the peak of the sound pressure and

the vibrational acceleration, it is observed that the pressure is larger than the acceleration at 1500 Hz, the former is smaller at 1750 and 3500 Hz, it is larger at 4000 Hz, and it is smaller at the frequency range above 4000 Hz.

The numerical calculation for the test web wheel which is engaged by the web (h=5.0 mm) and the rim (h=20.6 mm) is carried out. Table 5-1 shows the calculated $\bar{W}/\bar{H}$. The $\bar{W}/\bar{H}$ of the test web wheel is small and remains constant compared with those of the thin disks. The reason is explained as follows. Since the kinetic power is proportional to the thickness, the acoustic radiation coefficient of the web wheel, whose rim is considerably thick, is small. Also, the natural frequencies of the web wheel are determined by the shape of the rim. Thus, we may assume that the coincidence frequency is about 577 Hz, because f_c of a plate with 20.6 mm thickness is 577 Hz. The natural frequencies of the web wheel are much higher than f_c, therefore $\bar{W}/\bar{H}$ is small in its frequency range.

Then, we consider the real size wheel. When the wheels have similar shapes, the natural frequencies are inversely proportional to their size. Hence, in Eq. (5-7), $k=\omega/c$ is inversely proportional to the size, R is proportional to the size, and finally kR is constant. Therefore, it is noted that $\bar{W}$ does not depend on the size of the wheel. Also, in the similar manner, the mechanical vibrational power $\bar{H}$ is independent of the size. Then, the acoustic radiation coefficient of the resonant vibration is the same as the values which are shown in Table 5-1, in which the natural frequency is multiplied by 1/6.

5.4 Conclusions

When we deal with the noise from the thin wheel, we have to pay attention to the very low order modes and the modes whose natural frequencies are a little higher than the coincidence frequency because their acoustic radiation coefficients have large values. However, in the case of the web wheel, its coincidence frequency is lower than the natural frequencies, and it has no natural mode with significantly large acoustic radiation coefficient.

REFERENCES

1) Matsuhisa,H., & Sato,S., Bull.JSME, 22-173 (1979), 1626.
2) Stephens,R.W.B., & Bate,A.E., "Acoustic and Vibrational physics", Edward Arnold Ltd., (1966), 704.
3) Gösele,K., Acoustica, 3 (1953), 243.

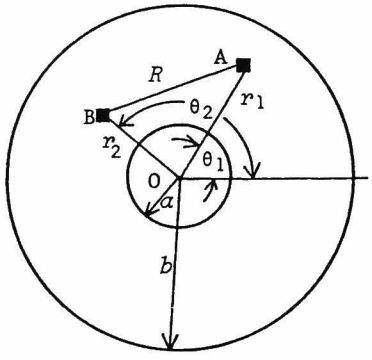

Fig. 5-1 Polar coordinates.

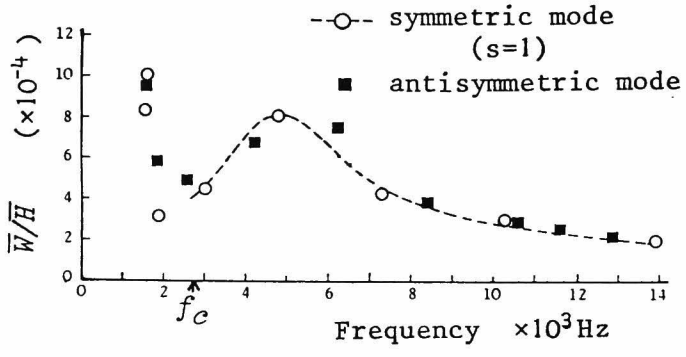

Fig. 5-2 Calculated $\overline{W}/\overline{H}$ of the disk with r_1=50 mm, r_2=150 mm, and h=5 mm.

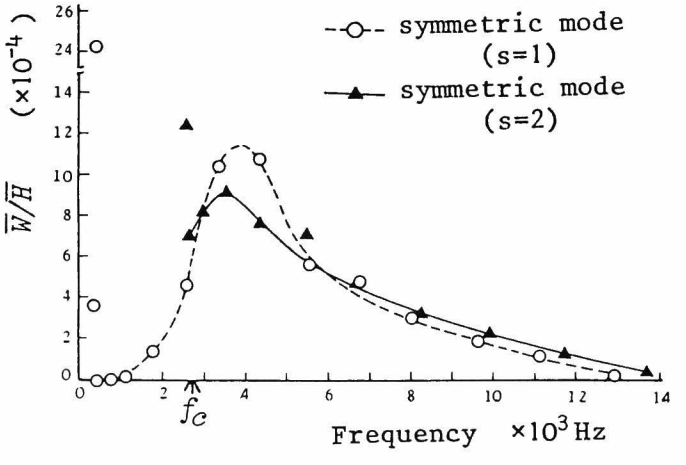

Fig. 5-3 Calculated $\overline{W}/\overline{H}$ of the disk with r_1=100 mm, r_2=300 mm, and h=5 mm.

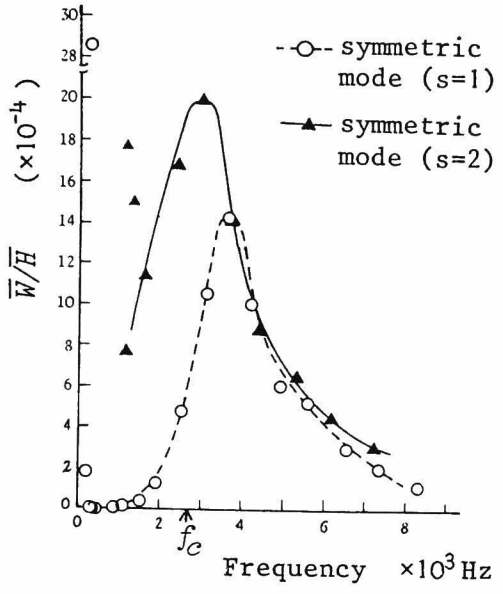

Fig. 5-4 Calculated $\overline{W}/\overline{H}$ of the disk with r_1=150 mm, r_2=450 mm, and h=5mm.

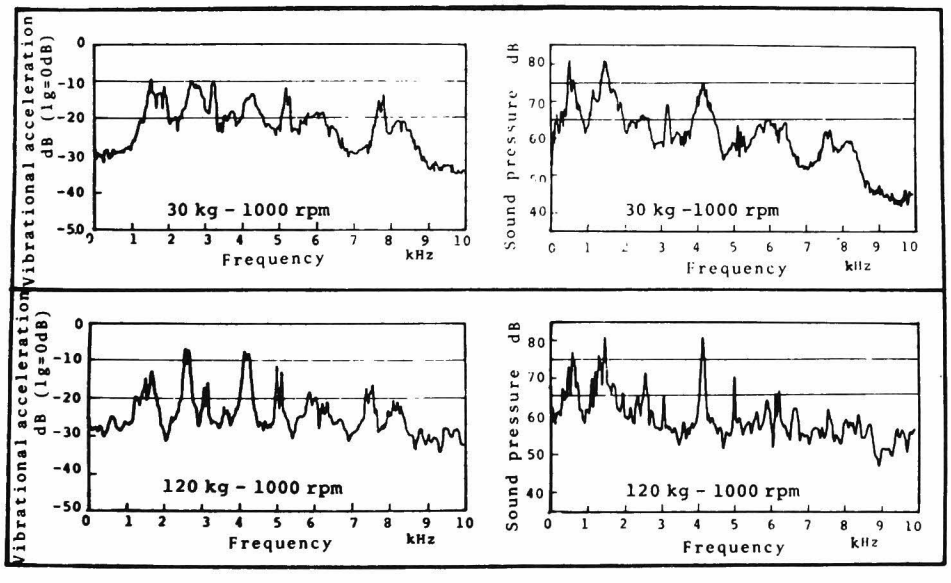

Fig. 5-5 Measured frequency spectra of the accceleration and the sound pressure of the thin disk.

Table 5-1 Calculated $\overline{W}/\overline{H}$ of the web wheel.

m,s	f(Hz)	$\overline{W}/\overline{H}(\times 10^{-4})$
1,0	954	6.18
0,0	1349	6.61
2,0	2305	5.75
3,0	6208	5.54
4,0	11300	5.73
5,0	17114	5.80
0,1	9140	15.85
1,1	9926	16.41
2,1	12084	17.35
3,1	15198	17.97
4,1	19164	18.45

CHAPTER 6 COUPLED VIBRATION OF WHEEL AND RAIL

6.1 Introduction

In the previous chapters, the vibration of the wheel was investigated. Since the wheel contacts with a rail, their coupled vibration is investigated in this chapter[1]. The emphasis is placed on the vibration of the wheel, and the rail is simulated by a beam with free ends. The contact condition between the wheel and the rail is rather complicated. However for the sake of simplification of the theoretical analysis, they are assumed to be connected by a spring. Under these assumptions, the coupled vibration is theoretically analyzed, including the effects of shear deformation and the rotatory inertia. Also, laboratory experiments are carried out with a model composed of the web wheel, the beam, and a connecting bolt, and the results are compared with the theoretical ones.

6.2 Theoretical Analysis

The basic equation for the vibration of the web wheel is the same as chapter 3. The equations of motion under an external force P_1 are given by

$$\frac{\partial M_r}{\partial r} + \frac{1}{r}\frac{\partial M_{r\theta}}{\partial \theta} + \frac{M_r - M_\theta}{r} - Q_r = \frac{\rho h^3}{12}\frac{\partial^2 \psi_r}{\partial t^2} , \tag{6-1}$$

$$\frac{\partial M_{r\theta}}{\partial r} + \frac{1}{r}\frac{\partial M_\theta}{\partial \theta} + \frac{2M_{r\theta}}{r} - Q_\theta = \frac{\rho h^3}{12}\frac{\partial^2 \psi_\theta}{\partial t^2} , \tag{6-2}$$

$$\frac{\partial Q_r}{\partial r} + \frac{1}{r}\frac{\partial Q_\theta}{\partial \theta} + \frac{Q_r}{r} + P_1 = \rho h \frac{\partial^2 w}{\partial t} . \tag{6-3}$$

Since the external force P_1 acts only on the contacting point (r_0, θ_0) with the rail, p_1 is expressed by Dirac's Delta function as

$$P_1 = P_{10}\delta(r-r_0)\delta\{r(\theta-\theta_0)\}e^{i\omega t} . \tag{6-4}$$

w, ψ_r, ψ_θ, M_r, $M_{r\theta}$, Q_r, and Q_θ are assumed to be given in the form of series of the eigenfunctions w_{ms}, $\psi_{r,ms}$, $\psi_{\theta,ms}$, $M_{r,ms}$, $M_{r\theta,ms}$, $Q_{r,ms}$, and $Q_{\theta,ms}$, which were obtained in chapter 3 as follows:

$$w = \sum_{ms} C_{ms} w_{ms} e^{i\omega t} , \quad \psi_r = \sum_{ms} C_{ms} \psi_{r,ms} e^{i\omega t}, \cdots \text{etc.} \tag{6-5}$$

where, C_{ms}'s are arbitrary constants which are determined in such a manner to satisfy the contact condition with the rail. Substituting Eq. (6-5) into Eqs. (6-1) to (6-3), the following Eqs. (6-6) to (6-8) are obtained.

$$\frac{\partial \sum C_{ms} M_{r,ms}}{\partial r} + \frac{1}{r}\frac{\partial \sum C_{ms} M_{r\theta,ms}}{\partial \theta} + \frac{\sum C_{ms} M_{r,ms} - \sum C_{ms} M_{\theta,ms}}{r} - \sum C_{ms} Q_{r,ms} = -\frac{\rho h^3}{12}\omega^2 \sum C_{ms}\psi_{r,ms} , \tag{6-6}$$

$$\frac{\partial \sum C_{ms} M_{r\theta,ms}}{\partial r} + \frac{1}{r}\frac{\partial \sum C_{ms} M_{\theta,ms}}{\partial \theta} + \frac{2\sum C_{ms} M_{r\theta,ms}}{r} - \sum C_{ms} Q_{\theta,ms} = -\frac{\rho h^3}{12}\omega^2 \sum C_{ms}\psi_{\theta,ms} , \tag{6-7}$$

$$\frac{\partial \sum C_{ms} Q_{r,ms}}{\partial r} + \frac{1}{r}\frac{\partial \sum C_{ms} Q_{\theta,ms}}{\partial \theta} + \frac{\sum C_{ms} Q_{r,ms}}{r} + P_{10}\delta(r-r_0)\delta\{r(\theta-\theta_0)\} = -\rho h\omega^3 \sum C_{ms} w_{ms} . \tag{6-8}$$

The eigenfunctions satisfy the homogeneous equations (P_1=0) of Eqs. (6-1) to (6-3) as,

$$\frac{\partial M_{r,ms}}{\partial r} + \frac{M_{r\theta,ms}}{\partial \theta} + \frac{M_{r,ms} - M_{\theta,ms}}{r} - Q_{r,ms} = -\frac{\rho h^3}{12} \omega_{ms}{}^2 \psi_{r,ms}, \tag{6-9}$$

$$\frac{\partial M_{r\theta,ms}}{\partial r} + \frac{1}{r}\frac{\partial Q_{\theta,ms}}{\partial \theta} + \frac{2M_{r\theta,ms}}{r} - Q_{\theta,ms} = -\frac{\rho h^3}{12} \omega_{ms}{}^2 \psi_{\theta,ms}, \tag{6-10}$$

$$\frac{\partial Q_{r,ms}}{\partial r} + \frac{1}{r}\frac{\partial Q_{\theta,ms}}{\partial \theta} + \frac{Q_{r,ms}}{r} = -\rho h \omega_{ms}{}^2 w_{ms} . \tag{6-11}$$

where ω_{ms} is the natural angular frequency.

Substitution of Eqs. (6-9) to (6-11) into Eqs. (6-6) to (6-8) gives

$$\sum_{ms} \rho \frac{h^3}{12} (\omega_{ms}{}^2 - \omega^2) C_{ms} \psi_{r,ms} = 0 , \tag{6-12}$$

$$\sum_{ms} \rho \frac{h^3}{12} (\omega_{ms}{}^2 - \omega^2) C_{ms} \psi_{\theta,ms} = 0 , \tag{6-13}$$

$$\sum_{ms} \rho h (\omega_{ms}{}^2 - \omega^2) C_{ms} w_{ms} = P_{10} \delta(r-r_0) \delta\{r(\theta-\theta_0)\} . \tag{6-14}$$

The eigenfunctions have the normal orthogonality[2] as

$$\int_0^{2\pi} \int_a^b \rho \left(\frac{h^3}{12} \psi_{r,ij} \psi_{r,n\ell} + \frac{h^3}{12} \psi_{\theta,ij} \psi_{\theta,k\ell} + h w_{ij} w_{k\ell} \right) r dr d\theta = \delta_{ij,k\ell}, \tag{6-15}$$

where a: inner radius, b: outer radius, and

$$\delta_{ij,kl} = \begin{cases} 1 & \text{for } i=k \text{ and } j=l \\ 0 & \text{for } i \neq k \text{ or } j \neq l. \end{cases}$$

Multiplying Eqs. (6-12) to (6-14) by $\psi_{r,ms}$, $\psi_{\theta,ms}$, and w_{ms}, respectively, summing all of them together, performing the integration over the plate surface, and making use of Eq. (6-15), the following equation is obtained.

$$(\omega_{ms}{}^2 - \omega^2) C_{ms} = P_{10} w_{ms}(r_0, \theta_0) \tag{6-16}$$

The displacement w is obtained by substituting Eq. (6-16) into Eq. (6-5) as

$$w(r,\theta) = \sum_{ms} \frac{w_{ms}(r,\theta)w_{ms}(r_0,\theta_0)}{(\omega_{ms}^2-\omega^2)} P_{10} \quad . \tag{6-17}$$

Finally, the displacement at the contact point is given by

$$w(r_0,\theta_0) = \sum_{ms} \frac{w_{ms}^2(r_0,\theta_0)}{(\omega_{ms}^2-\omega^2)} P_{10} \quad . \tag{6-18}$$

The rail is assumed to be a Timoshenko beam[3] which considers the effects of shear deformation and rotatory inertia. Let ψ denote the slope of the deflection curve when the shearing force is neglected, and β the angle of shear at the neutral axis in the same cross section, then we find for the complete slope

$$\frac{\partial y}{\partial x} = \psi + \beta \quad . \tag{6-19}$$

From the elementary theory of bending, we have for bending moment and shearing force the following equations.

$$M = EI \frac{\partial y}{\partial x} \quad , \tag{6-20}$$

$$V = - k'\beta AG = -k'\left(\frac{\partial y}{\partial x} - \psi\right) AG \quad . \tag{6-21}$$

in which, k' is a factor depending on the shape of the cross section; A is the cross sectional area; G is the transverse modulus of elasticity; and I is the moment of inertia. The differential equations of rotation and translatory motion in a vertical direction are

$$\frac{\partial M}{\partial x} - V = \rho I \frac{\partial^2 \psi}{\partial t^2} \quad , \tag{6-22}$$

$$-\frac{\partial V}{\partial x} + P_2 = \rho A \frac{\partial^2 y}{\partial t^2} \quad . \tag{6-23}$$

Since the external load P_2 acts only on the contact point (x_0) with the wheel, P_2 is expressed by

$$P_2 = P_{20}\delta(x-x_0)e^{i\omega t} \quad . \tag{6-24}$$

Let M, V, ψ, and y be given in the form of series of the eigenfunctions of the beam M_m, V_m, ψ_m, and y_m, respectively.

$$M = \sum_m C_m M_m e^{i\omega t}, \quad V = \sum_m C_m V_m e^{i\omega t}, \quad \cdots \text{ etc.} \tag{6-25}$$

Since these eigenfunctions are the solution of Eqs. (6-22) and (6-23) with P_2=0, the following equations are satisfied.

$$\frac{dM_m}{dx} - V_m = -\rho I\omega_m^2\psi_m \quad , \tag{6-26}$$

$$-\frac{dV_m}{dx} = -\rho A\omega_m^2 y_m \quad . \tag{6-27}$$

where ω_m is the natural angular frequency. Also the eigenfunctions have the normal orthogonality as

$$\int_0^l \rho(I\psi_i\psi_j + Ay_iy_j)dx = \delta_{ij} \quad . \tag{6-28}$$

Substitution of Eqs. (6-24) and (6-25) into Eqs. (6-26) and (6-27) yields

$$\sum_m \rho I(\omega_m^2-\omega^2)C_m\psi_m = 0 \quad , \tag{6-29}$$

$$\sum_m \rho A(\omega_m^2-\omega^2)C_m y_m = P_{20}\delta(x-x_0) \quad . \tag{6-30}$$

Multiplying Eqs. (6-29) and (6-30) by ψ_m and y_m, respectively, adding both together, and performing the integration over the whole length, the following equation is obtained.

$$(\omega_m^2 - \omega^2)C_m = P_{20}y_m(x_0) \quad . \tag{6-31}$$

Substituting C_m of this equation into Eq. (6-25), the displacement y is obtained.

$$y(x) = \sum_m \frac{y_m(x)y_m(x_0)}{(\omega_m^2-\omega^2)} P_{20} \quad . \tag{6-32}$$

Finally, the displacement at the contact point is given as

$$y(x_0) = \sum_m \frac{y_m^2(x_0)}{(\omega_m^2-\omega^2)} P_{20} \quad . \tag{6-33}$$

We assume that there exists a spring whose constant is k between the wheel and the rail. Then, the exteternal force P_{10} and P_{20} which work on the wheel and the rail, respectively, are given by

$$P_{10} = k\{-w(r_0,\theta_0) + y(x_0)\} \quad , \tag{6-34}$$

$$P_{20} = k\{-y(x_0) + w(r_0,\theta_0)\} \quad . \tag{6-35}$$

Substitution of Eqs. (6-34) and (6-35) into Eqs.(6-18) and (6-33) yields

$$w(r_0,\theta_0) = \sum_{ms} \frac{w_{ms}^2(r_0,\theta_0)}{(\omega_{ms}^2 - \omega^2)} k\{-w(r_0,\theta_0) + y(x_0)\} \quad , \tag{6-36}$$

$$y(x_0) = \sum_m \frac{y_m^2(x_0)}{(\omega_m^2 - \omega^2)} k\{-y(x_0) + w(r_0,\theta_0)\} \quad . \tag{6-37}$$

These equations are rewritten in a matrix form as

$$\begin{bmatrix} 1 + k\sum_{ms} \dfrac{w_{ms}^{2}(r_0,\theta_0)}{(\omega_{ms}^{2}-\omega^2)} & -k\sum_{ms} \dfrac{w_{ms}^{2}(r_0,\theta_0)}{(\omega_{ms}^{2}-\omega^2)} \\ -k\sum_{m} \dfrac{y_{m}^{2}(x_0)}{(\omega_{m}^{2}-\omega^2)} & 1 + k\sum_{m} \dfrac{y_{m}(x_0)}{(\omega_{m}^{2}-\omega^2)} \end{bmatrix} \begin{bmatrix} w(r_0,\theta_0) \\ y(x_0) \end{bmatrix} = \begin{bmatrix} 0 \\ 0 \end{bmatrix} \tag{6-38}$$

From the frequency equation obtained from Eq. (6-38), the natural angular frequency of the coupled vibration of the wheel and rail is obtained. Substitution of the natural angular frequency into Eqs. (6-17) and (6-32) gives the modes of vibration of the wheel and the rail.

6.3 Remarks on Experimental Procedure

In the practical system, the wheel contacts with the rail at the wheel's periphery. In this case, not only the force but also the moment acts on the beam at the contact point. In this chapter, the wheel and rail system is simplified as much as possible. To eliminate the moment, the rail is located at the side of the wheel as illustrated in Fig. 6-1. The rail is simulated by a beam with free ends. The wheel and the rail are connected by a bolt of M4. The spring constant k is varied by changing the length of the bolt.

The acceleration pick-ups are attached to the wheel and the rail. The acceleration under shock impulse is measured. Their frequency spectra are obtained by a real time, two channels frequency analyzer. In the beginning,

the wheel and the rail are separated and their shock response are measured. Then, both are connected, and the spectra are measured by taking the length of the connecting bolt and the location of the connection as variables. Finally, the modes of vibration are investigated by checking the phase lag at each point.

6.4 Results of Numerical Calculations and Measurements

6.4.1 Independent vibration of wheel and rail

The theoretical natural frequencies of the independent wheel and the rail are shown in Table 6-1. In this case, the wheel and the rail do not have any contact point. The experimental results are shown in Fig. 6-2. In the experimental result of the wheel the peaks at (0,1), (1,1), (4,1), and (0,2) modes which have circular nodes do not appear. This is due to the asymmetry of the experimental apparatus and the impulsing point not being at the center of the wheel. However, the other peaks at the natural frequencies of both of the results are in good agreement.

6.4.2 Coupled vibration of wheel and rail

When the connecting point is at the center of the beam and the connecting spring constant is 1.27×10^{8} N/m (1.3×10^{4} kgf/mm) the theoretical natural frequencies and their modes of vibration are shown in Fig. 6-3. In this figure, if the mode line of the beam is above the horizontal coordinate, the vibrational phase of the beam is the

same as that of the wheel at the connecting point; otherwise, the phase is reversed.

Figures 6-4 and 6-5 show the measured frequency spectrum, with the bolt length being 10mm and 6mm, respectively. When the location of the acceleration pick-ups and the impulsing point are varied, the peak levels change but the peak frequencies do not. In these figures, symbols A, B, C, etc. indicate the theoretical natural frequencies. The theoretical frequencies and the measured frequencies are in good agreement. Comparing Figs. 6-4 and 6-5, the peak frequencies in Fig. 6-5 are slightly higher than those in Fig. 6-4. This is because the connecting bolt of Fig. 6-5 is shorter than that of Fig. 6-4, consequently the spring constant k of the former is larger than that of the latter.

Table 6-2 shows the theoretical natural frequencies with three kinds of spring constant. The frequencies increase with an increase in the spring constant. However, the increasing rates of each natural frequencies are not similar. Some of them increase much, and some slightly. This is because the natural frequencies of the coupled vibration exist between the natural frequencies of the independent vibration of the wheel and the rail. Therefore, when the neighbouring natural frequencies are close to each other, the natural frequencies of the coupled vibration do not change much with the spring constant. When the spring constant is larger than 9.8×10^8 N/m, the natural frequencies are almost the same as the natural frequencies of the coupled vibration with $k=\infty$. When k decreases, the natural frequencies converge to the natural frequencies of the free independent vibration of the wheel

and the beam.

Figure 6-6 shows the theoretical natural frequencies and their modes of vibration when the connecting point is at a distance of 53 mm from the edge of the beam and $k=1.27\times10^{8}$ N/m. Figure 6-7 shows the experimental results of the shock response under the same condition as the theoretical results mentioned above (bolt length is 6 mm). In this figure, symbols A', B', C', etc. indicate the theoretical natural frequecies. Since the connecting point is not at the center of the beam, there are modes of vibration which have odd numbers of the nodal point in the beam. This can not be seen in the case when the connecting point is at the center of the beam.

The theoretical results are slightly different from the experimental ones. In the theoretical analysis, the moment at the connecting point is ignored. Therefore, if the moment is taken into consideration, the theoretical results are expected to be in a better agreement with the experimental results.

6.5 Conclusions

The coupled vibration of the wheel and the rail is investigated theoretically and experimentally by making use of a simple model which is composed of the web wheel , the beam with free ends, and the connecting bolt. The coupled vibration is analyzed under the assumptions that the web wheel is a Mindlin plate, the beam is a Timoshenko beam, and the connecting bolt is a spring. This theoretical analysis is confirmed by the experimental results. This method can be applied to the theoretical analysis of the

coupled vibration of the practical wheel and rail.

REFERENCES

1) Matsuhisa,H., et al., Proc.JSME, 815-2 (1981), 51.

2) Reismann,H., Trans.ASME, Ser.E, 35-3 (1968), 510.

3) Timoshenko,S., "Vibration Problems in Engineering", D.Van Nostrand Company Inc. (1928), 226.

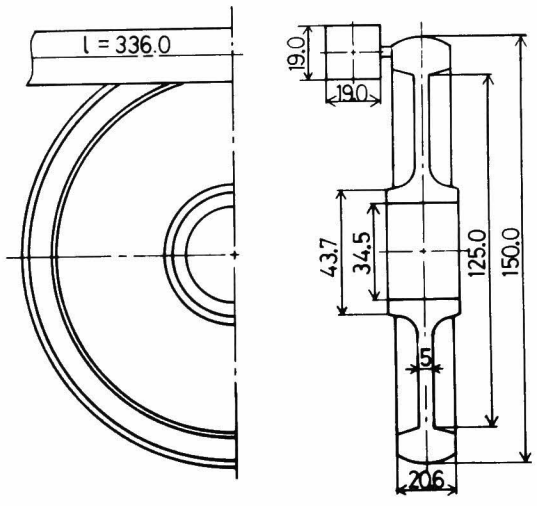

Fig. 6-1 Experimental wheel-rail system.

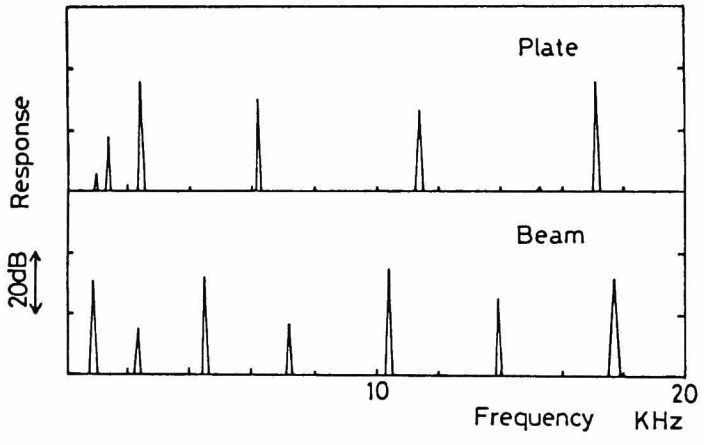

Fig. 6-2 Vibration spectra of the independent wheel and rail.

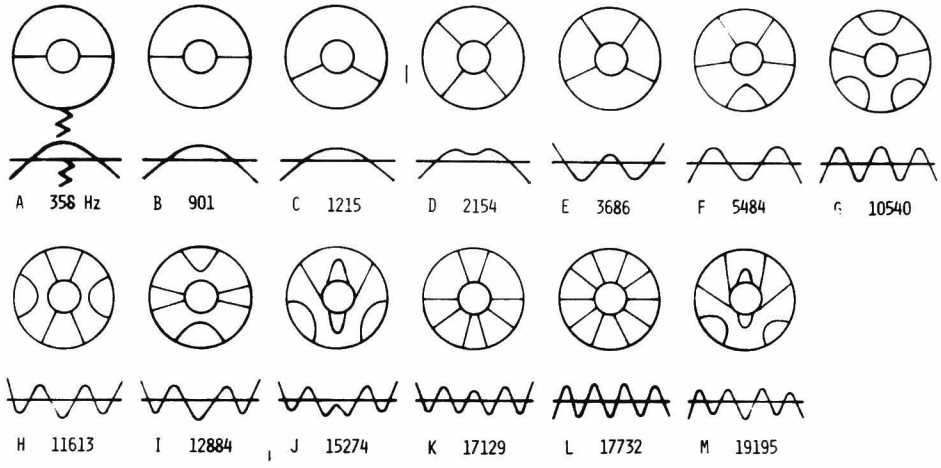

Fig. 6-3 Mode shapes of the wheel and the rail which are connected at the center of the rail.

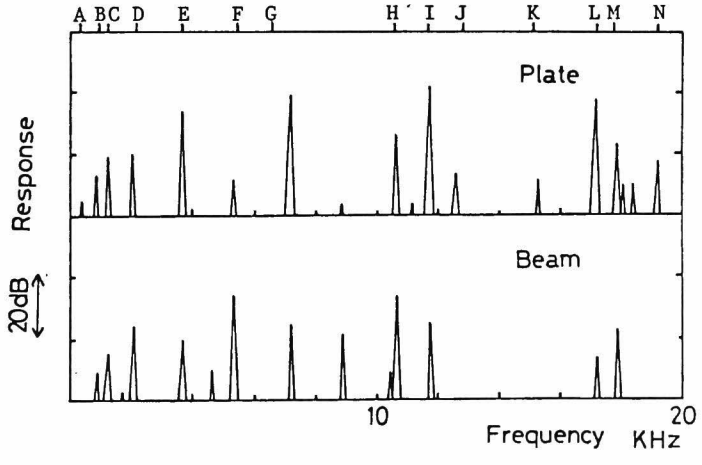

Fig. 6-4 Frequency spectra of the coupled vibration; connecting point : center of the rail, connecting bolt length : 10 mm.

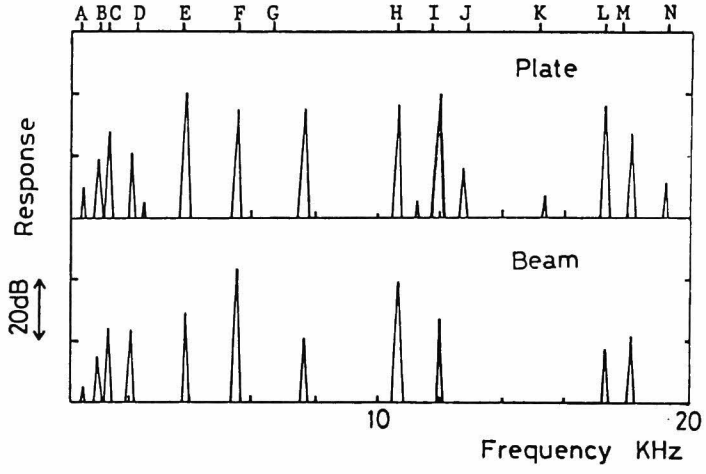

Fig. 6-5 Frequency spectra of the coupled vibration; connecting point : center of the rail, connecting bolt length : 6 mm.

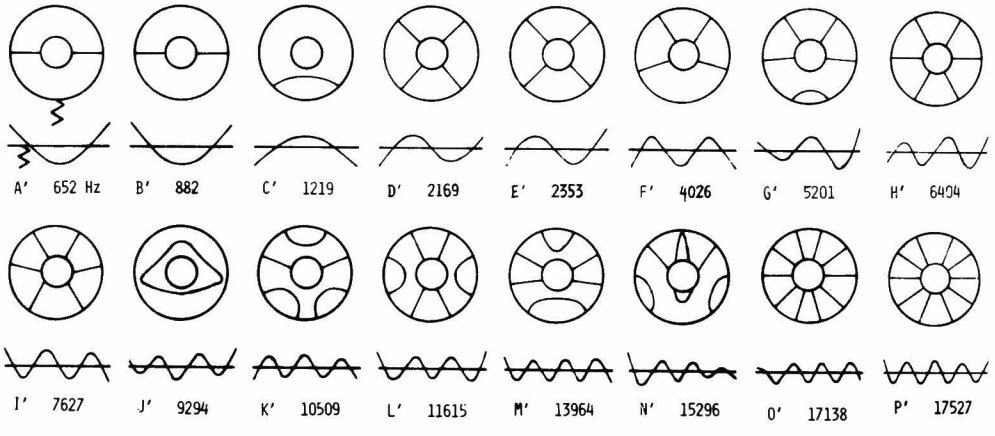

Fig. 6-6 Mode shapes of the wheel and the rail which are connected at 53 mm from the edge.

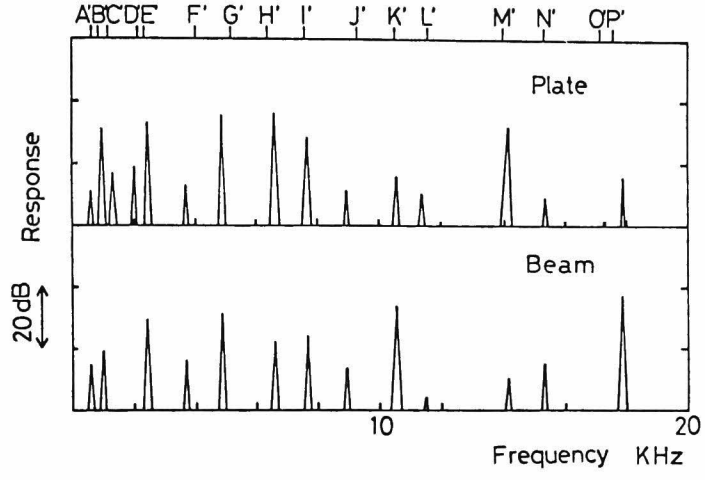

Fig. 6-7 Frequency spectra of the coupled vibration; connecting point : 53 mm from the edge, connecting bolt length : 6 mm.

Table 6-1 Theoretical natural frequencies of the independent wheel and rail.

Plate	(m,s)	Beam	(i)
954 Hz	(1,0)	873 Hz	(2)
1349	(0,0)	2357	(3)
2305	(2,0)	4491	(4)
6208	(3,0)	7168	(5)
9140	(0,1)	10290	(6)
9926	(1,1)	13766	(7)
11300	(4,0)	17519	(8)
12084	(2,1)		
15198	(3,1)		
17114	(5,0)		
19164	(4,1)		
19577	(0,2)		

Table 6-2 Theoretical natural frequencies of the coupled vibration.

$k=9.8\times10^{6}$N/m (1.0×10^{3}kg/mm)	9.8×10^{7} (1.0×10^{4})	9.8×10^{8} (1.0×10^{5})
300Hz	355	362
899	901	901
1164	1214	1218
1704	2147	2172
2397	3576	3961
4552	5303	5944
6223	6453	7711
10314	10499	10744
11331	11568	11768
12116	12634	14938
15202	15252	16364
17115	17126	17159
17533	17677	18598
19167	19189	19245

CHAPTER 7 VIBRATION OF A SPOKE WHEEL AND ITS NOISE REDUCTION

7.1 Introduction

In chapter 3, the vibration of the web wheel was investigated, and it was found that the vibration of the web is not negligible compared with that of the rim. The web generates considerablly large noise because of its large area. From this point of view, a spoke wheel is expected to reduce the noise.

In this chapter, the vibration of the spoke wheel is analyzed theoretically under the assumption that the spokes are springs which support the rim. The results of this analysis is compared with the experimental ones. Also, the noise caused by the spoke wheel is compared with that by the web wheel, and its characteristics of the noise reduction are investigated[1)].

7.2 Theoretical Analysis

Since the spokes of the wheel shown in Fig. 7-1 are assumed to be springs supporting the rim, the external force and the moments which act on the rim are given by;

$$\overline{P} = \sum_{\ell=1}^{8} P_\ell \delta(r-r_\ell)\delta\{r(\theta-\theta_\ell)\} \quad , \tag{7-1}$$

$$\overline{M}_r = \sum_{\ell=1}^{8} M_{r,\ell} \delta(r-r_\ell)\delta\{r(\theta-\theta_\ell)\} \quad , \tag{7-2}$$

$$\overline{M}_{r\theta} = \sum_{\ell=1}^{8} M_{r\theta,\ell} \delta(r-r_\ell)\delta\{r(\theta-\theta_\ell)\} \quad , \tag{7-3}$$

where $(r_l, \theta_l : l=1,2,\cdots,8)$ are support points.

The equations of motion of the rim become

$$\frac{\partial M_r}{\partial r} + \frac{1}{r}\frac{\partial M_{r\theta}}{\partial \theta} + \frac{M_r - M_\theta}{r} - Q_r + \bar{M}_r = \frac{\rho h^3}{12}\frac{\partial^2 \psi_r}{\partial t^2} , \tag{7-4}$$

$$\frac{\partial M_{r\theta}}{\partial r} + \frac{1}{r}\frac{\partial M_\theta}{\partial \theta} + \frac{2M_{r\theta}}{r} - Q_\theta + \bar{M}_{r\theta} = \frac{\rho h^3}{12}\frac{\partial^2 \psi_\theta}{\partial t^2} , \tag{7-5}$$

$$\frac{\partial Q_r}{\partial r} + \frac{1}{r}\frac{\partial Q_\theta}{\partial \theta} + \frac{Q_r}{r} + \bar{P} = \rho h \frac{\partial^2 w}{\partial t^2} . \tag{7-6}$$

Then, the deflection w, slopes ψ_r, ψ_θ, etc. are given in the form of a double series of the eigenfunctions of the rim with free inner and outer circumferences as,

$$W = \sum_{m,s} C_{ms} W_{ms} , \quad \Psi_r = \sum_{m,s} C_{ms} \psi_{r,ms} , \quad \Psi_\theta = \sum_{ms} C_{ms} \psi_{\theta,ms} , \quad \cdots\text{etc.} \tag{7-7}$$

By the same procedure as in the previous chapter, we obtain

$$C_{ms}(\omega_{ms}^2 - \omega^2) = \int_0^{2\pi}\int_a^b (\bar{P} W_{ms} + \bar{M}_r \psi_{r,ms} + \bar{M}_{r\theta}\psi_{\theta,ms}) r dr d\theta . \tag{7-8}$$

Substitution of Eqs. (7-1) to (7-3) into Eq. (7-8) gives

$$C_{ms} = \sum_l \{P_l W_{ms}(r_l,\theta_l) + M_{r,l}\psi_{r,ms}(r_l,\theta_l) + M_{r\theta,l}\psi_{\theta,ms}(r_l,\theta_l)\} / (\omega_{ms}^2 - \omega^2) . \tag{7-9}$$

Substituting Eq. (7-9) into Eq. (7-7), the deflection and the slopes are obtained as;

$$W = \sum_l (P_l G_{11l} + M_{r,l} G_{12l} + M_{r\theta,l} G_{13l}) , \tag{7-10}$$

$$\psi_r = \sum_l (P_l G_{21l} + M_{r,l} G_{22l} + M_{r\theta,l} G_{23l}) , \tag{7-11}$$

$$\psi_\theta = \sum_\ell \left(P_\ell G_{31\ell} + M_{r,\ell} G_{32\ell} + M_{r\theta,\ell} G_{33\ell}\right) , \qquad (7\text{-}12)$$

where

$$G_{11\ell}(r,\Theta;r_\ell,\Theta_\ell) = \sum_{ms} w_{ms}(r,\Theta) w_{ms}(r_\ell,\Theta_\ell)/(\omega_{ms}^2-\omega^2) ,$$

$$G_{12\ell}(r,\Theta;r_\ell,\Theta_\ell) = \sum_{ms} w_{ms}(r,\Theta) \psi_{r,ms}(r_\ell,\Theta_\ell)/(\omega_{ms}^2-\omega^2) ,$$

$$G_{13\ell}(r,\Theta;r_\ell,\Theta_\ell) = \sum_{ms} w_{ms}(r,\Theta) \psi_{\Theta,ms}(r_\ell,\Theta_\ell)/(\omega_{ms}^2-\omega^2) ,$$

$$G_{21\ell}(r,\Theta;r_\ell,\Theta_\ell) = \sum_{ms} \psi_{r,ms}(r,\Theta) w_{ms}(r_\ell,\Theta_\ell)/(\omega_{ms}^2-\omega^2) ,$$

$$G_{22\ell}(r,\Theta;r_\ell,\Theta_\ell) = \sum_{ms} \psi_{r,ms}(r,\Theta) \psi_{r,ms}(r_\ell,\Theta_\ell)/(\omega_{ms}^2-\omega^2) ,$$

$$G_{23\ell}(r,\Theta;r_\ell,\Theta_\ell) = \sum_{ms} \psi_{r,ms}(r,\Theta) \psi_{\Theta,ms}(r_\ell,\Theta_\ell)/(\omega_{ms}^2-\omega^2) ,$$

$$G_{31\ell}(r,\Theta;r_\ell,\Theta_\ell) = \sum_{ms} \psi_{\Theta,ms}(r,\Theta) w_{ms}(r_\ell,\Theta_\ell)/(\omega_{ms}^2-\omega^2) ,$$

$$G_{32\ell}(r,\Theta;r_\ell,\Theta_\ell) = \sum_{ms} \psi_{\Theta,ms}(r,\Theta) \psi_{r,ms}(r_\ell,\Theta_\ell)/(\omega_{ms}^2-\omega^2) ,$$

$$G_{33\ell}(r,\Theta;r_\ell,\Theta_\ell) = \sum_{ms} \psi_{\Theta,ms}(r,\Theta) \psi_{\Theta,ms}(r_\ell,\Theta_\ell)/(\omega_{ms}^2-\omega^2) .$$

Denoting the spring constants of the spoke in the z, ψ_r, and ψ_θ directions by k, k_r, and k_θ, respectively, the reactive force and the moments at the contact point is given by

$$P_\ell = - kW(r_\ell,\theta_\ell) , \qquad (7\text{-}13)$$

$$M_{r,\ell} = - k_r \psi_r(r_\ell,\theta_\ell) , \qquad (7\text{-}14)$$

$$M_{r\theta,\ell} = - k_\theta \psi_\theta(r_\ell,\theta_\ell) . \qquad (7\text{-}15)$$

Substituting Eqs. (7-10) to (7-12) into Eqs. (7-13) to (7-15), the following simultaneous equations for P_l, $M_{r,l}$, and $M_{r\theta,l}$ $(l=1,2,\cdots,8)$ are obtained.

$$\sum_{\ell=1}^{8}\begin{bmatrix} \frac{\delta_{n\ell}}{k}+G_{11n\ell} & G_{12n\ell} & G_{13n\ell} \\ G_{21n\ell} & \frac{\delta_{n\ell}}{k_\ell}+G_{22n\ell} & G_{23n\ell} \\ G_{31n\ell} & G_{32n\ell} & \frac{\delta_{n\ell}}{k_\theta}+G_{33n\ell} \end{bmatrix}\begin{Bmatrix} P_\ell \\ M_{r,\ell} \\ M_{r\theta,\ell} \end{Bmatrix} = 0$$

$$(\ n = 1,2,\cdots,8)$$

(7-16)

where, $G_{ijnl}=G_{ij}(r_n\ ,\theta_n\ ;\ r_l,\ \theta_l)$.

From the frequency equation which is derived from Eq. (7-16), the natural angular frequency of the spoke wheel is determined. Also, substituting the eigenvectors P_l, $M_{r,l}$, and $M_{r\theta,l}$ into Eqs. (7-10) to (7-12), the mode shape of vibration is obtained

Since the wheel contacts with a rail on its tread, the vibration of the practical wheel is complicated as discussed in chapter 6. However, only a simple model is discussed here. The rail is assumed to be a spring which works in the z direction. By the similar procedure as the above, the final equations of this case become

$$\sum_{\ell=1}^{8} \begin{bmatrix} \frac{\delta_{n\ell}}{k} + G_{11n\ell} & G_{12n\ell} & G_{13n\ell} & G_{11n0} \\ G_{21n\ell} & \frac{\delta_{n\ell}}{k_\ell} + G_{22n\ell} & G_{23n\ell} & G_{21n0} \\ G_{31n\ell} & G_{32n\ell} & \frac{\delta_{n\ell}}{k_\theta} + G_{33n\ell} & G_{31n0} \\ G_{110\ell} & G_{120\ell} & G_{130\ell} & \frac{1}{k} + G_{1100} \end{bmatrix} \begin{Bmatrix} P_\ell \\ M_{r,\ell} \\ M_{r\theta,\ell} \\ P_0 \end{Bmatrix} = 0$$

$$(n = 1,2,\cdots, 8)$$

(7-17)

where K is the spring constant which supports the wheel, and the suffix 0 represents the supprort point. From this frequency equation, the natural angular frequencies and their mode shapes can be obtained.

7.3 Comparison Between Results of Calculations and Experiments

7.3.1 Vibration of rim

Table 7-1 shows the calculated natural frequencies f_{ms}'s of the rim whose shape is shown in Fig. 7-1. The outside, midside and inside diameters, and the outer and inner thicknesses are 150.0 mm, 129.0 mm, 119.0 mm, 20.6 mm, and 8.7 mm, respectively. In this table, m denotes the number of nodal diameters, and the number of the circular node is 0 for all modes. Fig, 7-2 shows the measured shock response of the acceleration. These two results are in good agreement with each other.

7.3.2 Vibration of un-supported spoke wheel

In the case of the un-supported spoke wheel, there are two types of mode, S-type mode and A-type mode. The nodal line of the S-type mode passes through the neutral line of the spokes, and that of the A-type mode passes through a line equidistant from the adjacent spokes as shown in Fig. 7-3. The S- and A-type modes have the same frequency equation except for the mode with m=4, and they consequently have the same natural frequencies. We do not have the S-type mode with m=0.

Figures 7-4 to 7-6 show the relationship between the theoretical natural frequencies and the spring constants k, k_r, and k , respectively. In these figures, the abscissa, dimensionless spring constants κ, κ_r, κ_θ, are given by

$$\kappa = k/k_0,\ \kappa_r = k_r/k_{r0},\ \kappa_\theta = k\ /k_{\theta 0}, \qquad (7\text{-}18)$$

respectively, where, k_0, k_{r0}, and $k_{\theta 0}$ are the calculated static stiffness of the cantilever (length : 25.0 mm, width : 12.0 mm, thickness : 8.7 mm) which simulates the spoke.

As shown in these figures, the natural frequencies increase exponentially with the dimensionless spring constants. From the restriction of the wheel's shape, the dimensionless spring constants may be in a range of 10^{-1} to 10^{1}. In this range, the lower order modes are sensitive to κ.

Figure 7-7 shows the measured shock response of the acceleration. From the calculated and the measured natural frequencies, the dimensionless spring constants can be assumed to be 0.4. The calculated natural frequencies with these values are shown in Table 7-2. The calculated fre-

quencies of the lower order modes differ from the measured frequencies. The beam is assumed to be a cantilever in the theoretical analysis; however, the spokes of the wheel are elastically supported at the inner ends. Thus, the difference between the theoretical and the experimental results are derived.

7.3.3 Vibration of supported spoke wheel

When the wheel is elastically supported at one point of the tread in the z direction, the vibration has two types of mode. One is a mode whose nodal line passes through the support point, while the nodal line of the other does not. The former is named S'-type, and the latter A'-type. When the support point is on the spoke diameter or is equidistant from the two adjacent spoke diameter, the S-type and A-type modes obtained in the previous section coincide with the S'-type modes. Therefore, in this section only the A'-type mode is discussed.

The relation between the natural frequencies and the spring constant K is shown in Fig. 7-8 for the case where the contact point is on the spoke diameter. As shown in this figure, the natural frequencies have a large increse at $K \cong 10^8$ N/m. When K decreases, the natural frequencies approach to those of the un-supported wheel, and when K increases they become close to those of simply supported wheel. The mode shapes slighty vary with K. The natural frequencies slightly depend on the location of the support. The measured shock responses of the wheel which contact with the guide wheel are shown in Figs. 7-9 and 7-10. Figure 7-9 shows the case that the contact point is

on the spoke diameter. Figure 7-10 shows the case that the contact point is just between the adjacent spoke diameters. When the load is changed, the peaks hardly change the position. The peaks appear at 1150, 2450, 6250, 12350, and 17100 Hz, which correspond to the S'-type modes, and 2050, 4250, 7100, 11650, and 17550 Hz which correspond to the A'-type modes. The peak at 3600 Hz is caused by a natural vibration of the guide wheel. One of the peaks at 1500 and 1750 Hz is supposed to be the S'-type mode and the other A'-type mode. However, it is difficult to distinguish them in this experiment because their frequencies are too close to each other. Comparing Figs. 7-9 and 7-10, the location of the peaks about 11000 Hz are slightly different. This is because the natural frequencies of S-type and A-type modes with m=4 are not equal. These measured frequencies are slightly different from the calculated frequencies. However, this can be improved by choosing the values of the spring constants of the spokes adequately.

The practical wheel is supported by a rail not only in the z direction, but also in other directions. Also, the spring constant K varies with the load and the frequency. However, for the experimental apparatus, the assumptions in this chapter are considered to be adequate to discuss the characterestics of the vibration of the spoke type wheel.

7.3.4 Running experiment

Figures 7-11 and 7-12 show the frequency spectra of the acceleration and the sound pressure of the wheel running with the guide wheel which has plane periphery. The

rotational speed and the load which are taken for this experiment are 1000 rpm and 300 N, respectively. In this experiment, even if the rotational speed and the load are changed, the locations of the peaks do not vary. The peaks of the acceleration spectrum in Fig. 7-11 are due to the S'-type modes. The peaks of the sound pressure are due to the S'-type modes, in-plane vibration of the wheel, and the vibration of the guide wheel. The total levels of the acceleration and the sound pressure increase with the rotational speed.

The exciting force which causes the transverse vibration of the wheel is generated at the contact point with the rail. The exciting force in the radial direction is much larger than that in the axial direction. The spoke wheel has larger exciting force in the radial direction than the web wheel because of its shape. Also, the corrugation and roughness of the rolling surface which cause the initiation of the exciting force are not constant for wheels. Therefore, by this experimental method, it is difficult to compare the noise levels of the spoke wheel and the web wheel.

Then, to simulate the condition that the train is traversing the curves, the experimental apparatus is set to have an angle α between the wheel and the guide wheel as shown in Fig. 4-1. By this method, the exciting force in the axial direction can be increased. The vibration with $\alpha=2.7$ is larger than that with $\alpha=0$ by about 10 dB.

In order to investigate the levels at arbitrary frequency, a guide wheel which has grooves (width : 0.2 mm, depth : 0.2 mm, interval : 1.1 mm) on its periphery, as

shown in Fig. 7-13, is used. With this grooved guide wheel, the vibration and noise levels of different wheels can be compared, because the amplitude of the vibration depends on the condition of the contact surface, and the grooves of the guide wheel is large enough to ignore the corrugation and roughness of the wheel surface. The frequency of the exciting force is denoted by f_z (f_z=NZ, N : number of rotation, Z : number of grooves). By making use of this grooved guide wheel with α=2.7 , the vibration and noise levels of the running wheels were measured.

The vibration and noise levels increase with f_z, and have large peaks of 20 to 30 dB at $f_z=f_{ms}$. At $f_z=f_{ms}/2$, the levels also have peaks, but they are much smaller than those at $f_z=f_{ms}$. Only the spoke wheel has small peaks when f_z coincides with the natural frequency of the in-plane vibration.

In order to compare the vibration and noise levels of the spoke wheel and the web wheel, the peak levels of the lower order modes, f_{20}= 2450 Hz, and f_{30}=6250 Hz which are dominant in the sound radiation at curves, are shown in Table 7-3. As seen in this Table, the vibration of the spoke wheel is smaller than that of the web wheel by 2 to 3 dB. Also, the noise of the spoke wheel is smaller than that of the web wheel by several dB.

7.4 Conclusions

In this chapter, the transverse vibration of the spoke wheel has been analyzed theoretically. Also, using a small model wheel, experimental observations were carried out. The results can be summarized as follows.

i) The vibration of the wheel can be theoretically analyzed by assuming the spokes to be springs which support the rim.

ii) When the wheel contacts with the guide wheel, the guide wheel may be assumed to be a spring in the theoretical analysis. The vibration has two types of mode, S'-type and A'-type modes. Both appear in the non-running experiment, but the S'-type mode is dominant in the running experiment.

iii) The noise radiated from the spoke wheel is smaller than that from the conventional web wheel by several dB, because the spoke wheel has smaller area of sound radiation.

REFERENCE

1) Matsuhisa,H., et al., Proc.JSME, 824-9 (1982), 25.

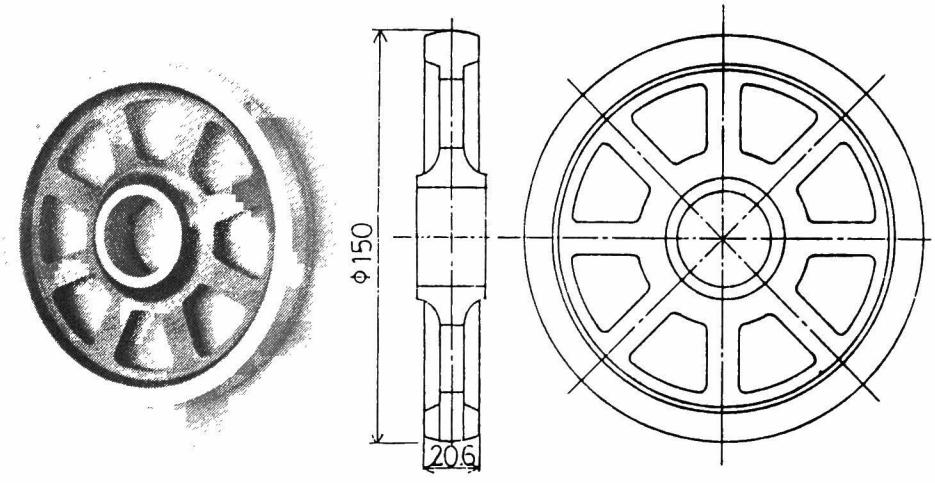

Fig. 7-1 Spoke wheel.

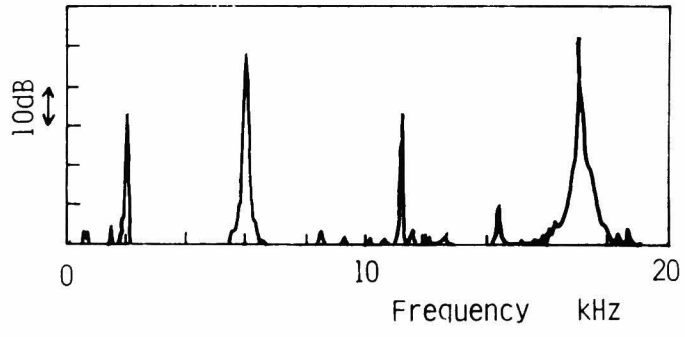

Fig. 7-2 Vibration spectrum of the rim.

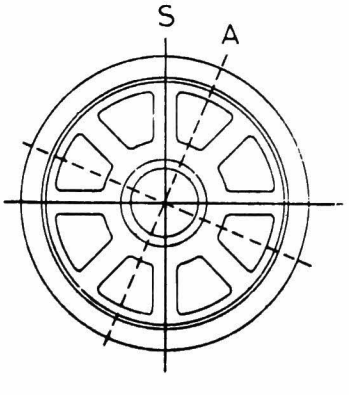

Fig. 7-3 S-type and A-type modes.

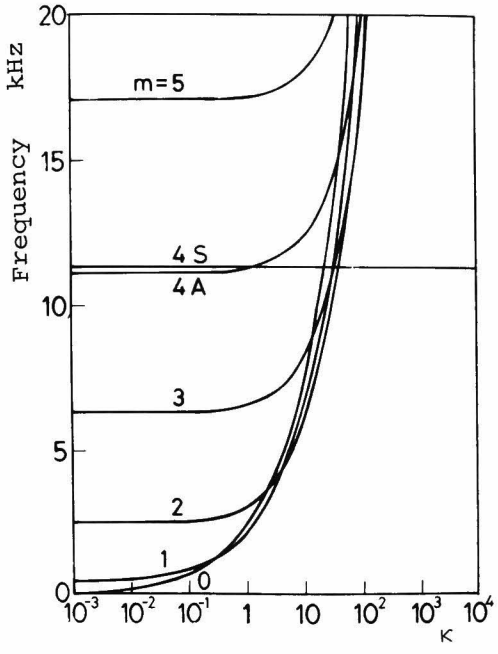

Fig. 7-4 Relation between the natural frequencies and κ.

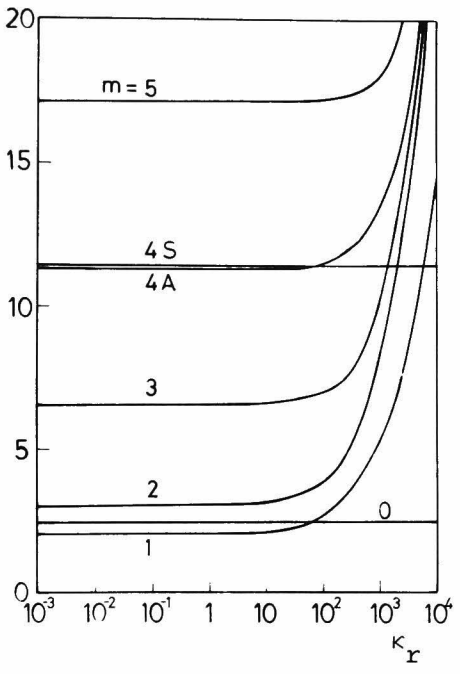

Fig. 7-5 Relation between the natural frequencies and κ_r.

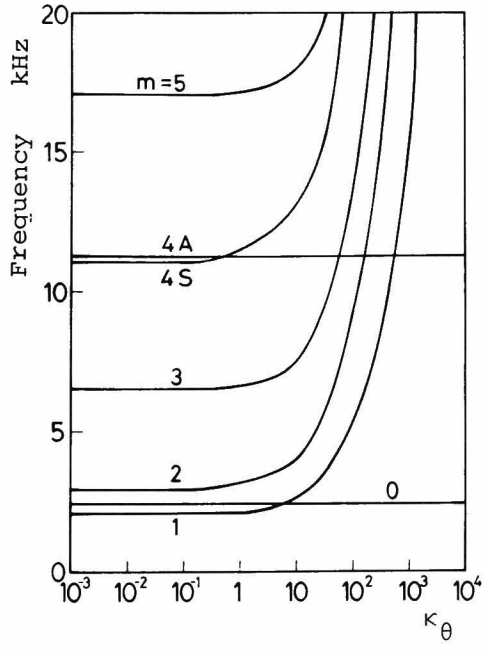

Fig. 7-6 Relation between the natural frequencies and κ_θ.

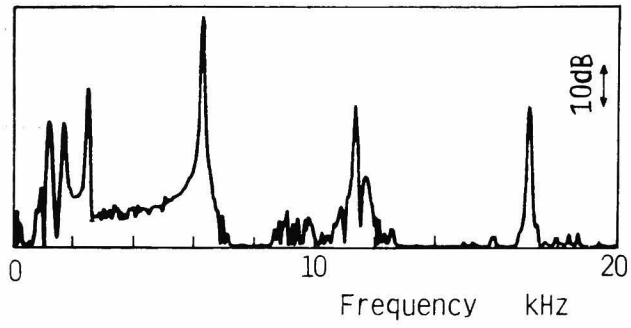

Fig. 7-7 Vibration spectrum of the spoke wheel.

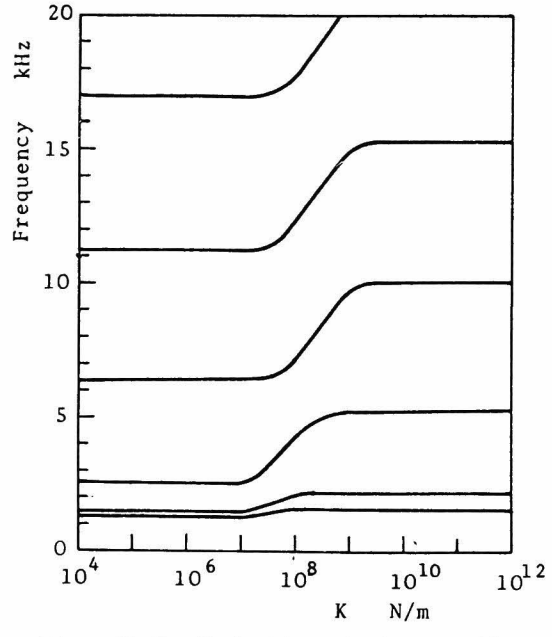

Fig. 7-8 Relation between the natural frequencies and K.

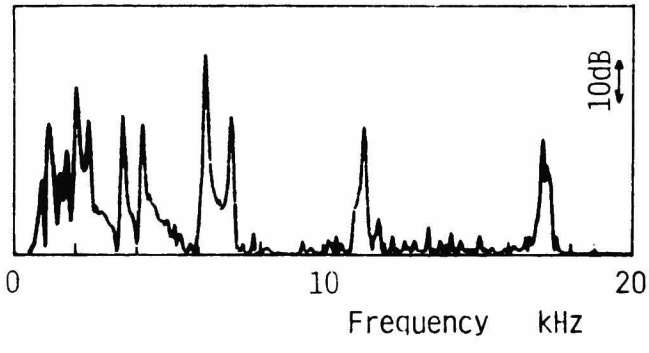

Fig. 7-9 Vibration spectrum of the spoke wheel which contact with the guide wheel; contact point is on the spoke diameter.

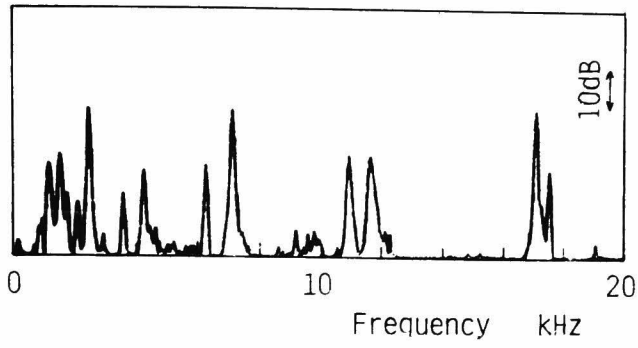

Fig. 7-10 Vibration spectrum of the spoke wheel which contact with the guide wheel; contact point is equidistant from the adjacent spoke diameters.

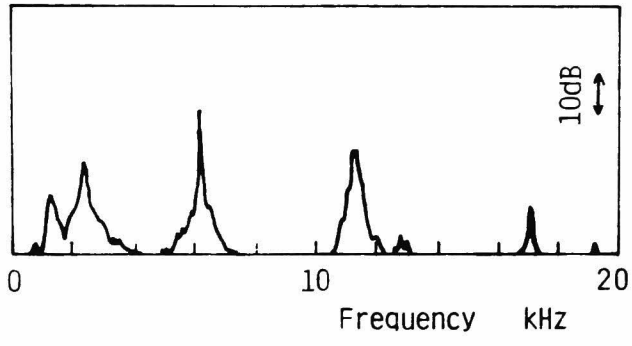

Fig. 7-11 Vibration spectrum of the rolling spoke wheel.

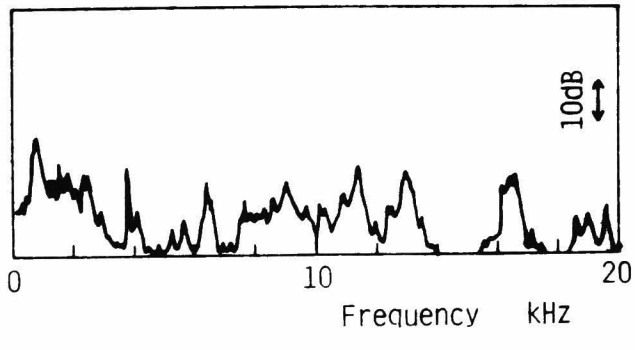

Fig. 7-12 Noise spectrum of the rolling spoke wheel.

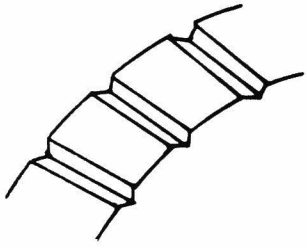

Fig. 7-13 Grooved guide wheel.

Table 7-1 Theoretical natural frequencies of the rim.

m	2	3	4	5
f (Hz)	2273	6190	11180	16951

Table 7-2 Theoretical natural frequencies of the spoke wheel.

m	0	1	2	3	4-S	4-A	5
f (Hz)	1548	1367	2610	6334	11260	11280	17024

Table 7-3 Vibration and noise levels of the rolling spoke wheel and web wheel.

		Spoke wheel	Web wheel
2450 Hz	V	82 dB	85
	N	80	91
6250	V	88	90
	N	88	94

CHAPTER 8 VIBRATION OF A DAMPED WHEEL AND ITS NOISE REDUCTION

8.1 Introduction

There are the spoke wheels, resilient wheels, and damped wheels, which generate less noise than the conventional web wheel. The spoke wheel, mentioned in the previous chapter, is expected to reduce the noise considerably. The resilient wheel, whose rim and hub are connected by a damping material, can also reduce the noise[1,2,3]. However, it is difficult to use the resilient wheel in practice due to its structural strength and cost. The damped wheel is composed of a main wheel and a vibration absorber attached to the side of the main wheel. This has been experimentally studied by several researchers[4,5], but there has been no theoretical study so far.

In this chapter, the damped wheel is investigated theoretically and experimentally[6]. The absorber is composed of a thin annular steel plate and a damping material (rubber) which are attached to the web. When the damped wheel flexurally vibrates in the axial direction, there exist shear forces among the main wheel, the rubber, and the plate, and damping of the rubber works not only in the z direction but also in the r and θ direction. However, in order to simplify the mathematical procedure of the theoretical analysis, the force is assumed to act only in the z direction, and the rubber's mass is neglected. On these assumptions, the transverse vibration of the damped wheel is analyzed.

Several models of a damped wheel are constructed, and

the characteristics of their vibration and noise are investigated experimentally. Especially, the relations between the vibration and the noise reductions and the structure of the absorber are investigated.

8.2 Theoretical Analysis

In this chapter, the loss factor is introduced to discuss quantitatively the vibration of various damped wheels shown in Fig. 8-1. In the beginning, the vibration of the main wheel is analyzed. Let the complex Young's modulus E* and the shear modulus G* be given as,

$$E^*=E(1+i\zeta),\quad G^*=G(1+i\zeta), \tag{8-1}$$

where ζ is loss factor. Then, the moments and the shear forces in the Mindlin plate[7] are given by

$$\begin{aligned} &M_r^*=M_r(1+i\zeta),\quad M_\theta^*=M_\theta(1+i\zeta),\quad M_{r\theta}^*=M_{r\theta}(1+i\zeta),\\ &Q_r^*=Q_r(1+i\zeta),\quad Q_\theta^*=Q_\theta(1+i\zeta). \end{aligned} \tag{8-2}$$

The equations of motion are

$$\left.\begin{aligned} &\frac{\partial M_r^*}{\partial r}+\frac{1}{r}\frac{\partial M_{r\theta}^*}{\partial \theta}+\frac{M_r^*-M_\theta^*}{r}-Q_r^*=\frac{\rho h^3}{12}\frac{\partial^2\psi_r}{\partial t^2},\\ &\frac{\partial M_{r\theta}^*}{\partial r}+\frac{1}{r}\frac{\partial M_\theta^*}{\partial \theta}+\frac{2M_{r\theta}^*}{r}-Q_\theta^*=\frac{\rho h^3}{12}\frac{\partial^2\psi_\theta}{\partial t^2},\\ &\frac{\partial Q_r^*}{\partial r}+\frac{1}{r}\frac{\partial Q_\theta^*}{\partial \theta}+\frac{Q_r^*}{r}+P_1 e^{i\omega t}=\rho h\frac{\partial^2 w}{\partial t^2}. \end{aligned}\right\} \tag{8-3}$$

The deflection w and others are assumed to be given in the series of their eigenfunctions w_{ms} and others as,

$$w=\sum_{ms} C_{ms} w_{ms} e^{i\omega t}, \quad \psi_r=\sum_{ms} C_{ms} \psi_{r,ms} e^{i\omega t}, \text{ etc..} \tag{8-4}$$

Substituting these into Eq. (8-3), and by the similar procedure as in the previous chapter, the following equation is obtained.

$$(\omega_{ms}{}^{*2}-\omega^2)C_{ms}=\int\int P w_{ms} r dr d\theta, \tag{8-5}$$

where $\omega_{ms}{}^{*2}=\omega_{ms}{}^2(1+i\zeta)$.

We can also have the following equation for the plate by the same procedure.

$$(\omega'^*_{nt}{}^2-\omega^2)C'_{nt}=\int\int P' w'_{nt} r dr d\theta, \tag{8-6}$$

where, suffix ' represents the plate.

The external forces P and P' are the reacting forces by the rubber, so they are shown as,

$$P=-P'=k^*(w'-w)=k^*(\sum_{nt} C'_{nt} w'_{nt}-\sum_{ms} C_{ms} w_{ms}), \tag{8-7}$$

where $k^*=k(1+i\eta)$, k:spring constant of the rubber, and η: loss factor of the rubber. Since the integration area of Eqs. (8-5) and (8-6) is the surface of the plate, substitution of Eq. (8-7) into these equations gives

$$(\omega^*_{ms}{}^2-\omega^2)C_{ms}=k^*\int_0^{2\pi}\int_{r_1}^{r_2}(\sum_{pg} C'_{pg} w'_{pg}-\sum_{ij} C_{ij} w_{ij}) w_{ms} r dr d\theta, \tag{8-8}$$

$$(\omega'^*_{nt}{}^2-\omega^2)C'_{nt}=k^*\int_0^{2\pi}\int_{r_1}^{r_2}(\sum_{ij} C_{ij} w_{ij}-\sum_{pg} C'_{pg} w'_{pg}) w'_{nt} r dr d\theta. \tag{8-9}$$

The eigenfunctions are given in the form as,

$$w_{ms}(r,\theta)=W_{ms}(r)\cos m\theta. \tag{8-10}$$

The Eqs. (8-9) can be rewritten as

$$(\omega^*_{ms}{}^2-\omega^2)C_{ms}=k^*\Pi_m(\Sigma_g C'_{mg}\int_{r_1}^{r_2}W'_{mg}W_{ms}rdr-\Sigma_j C_{mj}\int_{r_1}^{r_2}W_{mj}W_{ms}rdr), \tag{8-11}$$

$$(\omega'^*_{nt}{}^2-\omega^2)C'_{nt}=k^*\Pi_m(\Sigma_j C_{mj}\int_{r_1}^{r_2}W_{mj}W'_{mt}rdr-\Sigma_g C'_{mg}\int_{r_1}^{r_2}W'_{mg}W'_{nt}rdr), \tag{8-12}$$

where $\Pi_m=\int_0^{2\pi}\cos^2 m\theta d\theta=\begin{cases}2\pi & (m=0)\\ \pi & (m\geqq 1).\end{cases}$ (8-13)

Let $I_m(i,j)=\Pi_m\int_{r_2}^{r_2}W_{mi}W_{mj}rdr,$ (8-14)

$$J_m(i,j)=\Pi_m\int_{r_1}^{r_2}W'_{mi}W'_{mj}rdr, \tag{8-15}$$

$$L_m(i,j)=\Pi_m\int_{r_1}^{r_2}W_{mi}W'_{mj}rdr. \tag{8-16}$$

Then, Eqs. (8-11) and (8-12) are rewritten in a matrix form as,

$$A\mathbb{C}=\omega^2\mathbb{C}, \tag{8-17}$$

where $\mathbb{C}=(C_{m1}, C_{m2},\cdots, C'_{m1}, C'_{m2},\cdots)^T$,

$$A=\begin{pmatrix} k^*I_m(1,1)+\omega^*_{m1}{}^2 & k^*I_m(1,2) & \cdots & -k^*L_m(1,1) & -k^*L_m(1,2) & \cdots\\ k^*I_m(2,1) & k^*I_m(2,2)+\omega^*_{m2}{}^2 & \cdots & -k^*L_m(2,1) & -k^*L_m(2,2) & \cdots\\ \vdots & \vdots & & \vdots & \vdots & \\ -k^*L_m(1,1) & -k^*L_m(2,1) & \cdots & k^*J_m(1,1)+\omega'^*_{m1}{}^2 & k^*J_m(1,2) & \cdots\\ -k^*L_m(1,2) & -k^*L_m(2,2) & \cdots & k^*J_m(2,1) & k^*J_m(2,2)+\omega'^*_{m2}{}^2 & \cdots\\ \vdots & \vdots & & \vdots & \vdots & \end{pmatrix}.$$

The complex natural frequency $\omega=\Omega+i\beta$ is obtained by solving the above set of equations.

Now, we consider the displacement under the external force $P_0 e^{i\omega t}$ which acts on the rim (r_0,θ_0). In the following equations, the time term $e^{i\omega t}$ will be omitted. The external force is given by

$$P=k^*(w'-w)+P_0\delta(r-r_0)\delta\{r(\theta-\theta_0)\}. \tag{8-18}$$

In this case, Eq. (8-11) becomes

$$(\omega^*_{ms}{}^2-\omega^2)C_{ms} = k^*\Pi_m(\Sigma_g C'_{mg}\int_{r_1}^{r_2} W'_{mg}W_{ms}rdr-\Sigma_j C_{mj}\int_{r_1}^{r_2} W_{mj}W_{ms}rdr)$$
$$+P_0 w_{ms}(r_0,\theta_0) . \tag{8-19}$$

The equation for the plate under the external force is the same as Eq. (8-12), except ω is replaced by Ω. These two equations can be rewritten in the following matrix form.

$$A'\mathbb{C}=\mathbb{B} , \tag{8-20}$$

where $A'=A-\Omega^2 E$ (E:unit matrix) ,

$$\mathbb{B}=P_0\{w_{m1}(r_0,\theta_0),\ w_{m2}(r_0,\theta_0),\cdots,0,\ 0,\cdots\}^T.$$

From this simultaneous equation, the coefficients C_{ms} and C'_{nt} are determined. Substituting these coefficients into Eq. (8-4), the deflections w and w' under the external force are obtained.

8.3 Results of Numerical Calculations

The numerical caluculation for the damped wheel shown in Fig. 8-1 was carried out with $\zeta=3.0\times10^{-3}$ and $P_0=9.8$N. Table 8-1 shows the dominant natural frequencies f_{ms} of the main wheel. The natural frequencies of the damped wheel depend slightly on the structural shape of the absorber, i.e. thickness of the rubber h_r, thickness of the plate h_p,

inner and outer radii of the absorber r_1 and r_2. Only when the fundamental frequency f_{pr} of the absorber

$$f_{pr}=\frac{1}{2\pi}\sqrt{\frac{E_r}{h_r h_p \rho_p}} \tag{8-21}$$

(E_r:rubber's Young's modulus, ρ_p:plate's density)

is in the vicinity of f_{ms}, the natural frequency of the damped wheel is divided into two.

Figure 8-2 shows the relation between the acceleration levels of each mode and f_{pr}, in which the loss factor of the rubber $\eta=0.5$, $r_1=31.0$ mm, and $r_2=61.0$ mm. In this figure, 0 dB represents the acceleration of the wheel without the absorber, and the symbols A, B, C, D, E, F indicate the modes shown in Table 8-1.

Here, we compare the vibration amplitudes and the phases of the main wheel and the plate. When $f_{pr}=f_{ms}$, the plate has larger vibration than the main wheel. In the other region, the main wheel has larger vibration. Concerning the phase, at $f_{pr}<f_{ms}$, both have the same phases, at $f_{pr}\fallingdotseq f_{ms}$, the phase lag begins to appear and it increases with f_{pr}. This tendency depends on the loss factor η. When η increases, the phase lag curve has a gentle slope.

When η increases, the vibration is reduced. One example of the relation between the acceleration level and is shown in Fig. 8-3, in which $E_r=4.9\times10^8$ N/m^2, $r_1=31.0$ mm, $r_2=61.0$ mm, $h_p=4.0$ mm, and $h_r=5.0$ mm. In this case, $f_{pr}=8900$ Hz. The mode whose natural frequency is near f_{pr} remarkably decreases in the acceleration level.

8.4 Experimental Results and Discussions

Table 8-2 shows the shapes of the plate and the rubber which are used in the experiment. The experiment has two steps, non-running and running experiments. In the non-running experiment, the rim is sinusoidally excited by a electromagnetic exciter. Since the exciter contacts with wheel, the frequency spectrum slightly differs from that of the wheel alone. For example, a peak at 3000 Hz appears only in the coupled vibration of the wheel and the exciter. Since the D, E, and F modes are dominant in the radiated noise, mainly these modes are discussed here.

8.4.1 Non-running experiment

The acceleration level of a wheel only with the rubber is shown in Fig. 8-4. In this experiment, natural and nitrile rubbers are used, and the wheel of this type is named as a rubber coated wheel. In this figure and the following figures, the ordinate is set as 1g=0dB, and W_{st} represents the wheel without the absorber. Figure 8-5 shows the acceleration levels of the wheel with the absorber (PA, RA).

As shown in Fig. 8-4, the vibration of the rubber coated wheel is slightly smaller than that of the standard web wheel. However, the wheel with the absorber has smaller vibration especially at the high order modes as shown in Fig. 8-5. In Fig. 8-5, we can see that the nitrile rubber has larger damping effect than the natural rubber, except in the case of the D mode. This is explained by the loss factor of the nitrile rubber being greater than that of the natural rubber. This corresponds to the theoretical prediction, shown in Fig. 8-3, that the vibra-

tion decreases with the loss factor. At the D mode, f_{pr} of the natural rubber is in the vicinity of f_{30}, and its vibration remarkably decreases.

Figure 8-6 shows the difference in the acceleration between the absorbers (PA, RA) and (PA,RB) to investigate the effect of the natural rubber's thickness. The wheel with rubber RA (5 mm thickness) has smaller vibration than the wheel with RB (2 mm thickness) in the low order modes, and it is opposite in the high order modes. Because f_{pr} of the wheel with RA is in the low frequency region, and f_{pr} of the wheel with PB is in the higher frequency region.

Regarding the nitrile rubber, the same experiment is carried out. The results show that the vibration decreases with the rubber's thickness, but f_{pr} does not have so clear effect as the natural rubber.

From the above experiments, we find that the nitrile rubber is more effective for the vibration reduction than the natural rubber. Therefore, in the following experiment, only the nitrile rubber is used.

We investigate the effects of the inner and the outer radii of the absorber. Three kinds of the damped wheel are built, W_1 (PA, RA) whose absorber is attached to the whole area of the web, W_2 (PC, RC) whose absorber is attached to the outer half area of the web, and W_3 (PD, RD) whose absorber is attached to the inner half area of the web. Figure 8-7 shows the experimental results of these wheels. As shown in this figure, W_1 and W_2 have smaller vibration than W_3, especially at the high order modes.

Table 8-3 shows the theoretically calculated vibrational levels of these three wheels. This corresponds to the experimental results. From this we can conclude that

the absorber should be located as much outside of the web as possible.

The vibration amplitudes and the phases of the main wheel and the plate of three damped wheels W_1 (PA, RA), W_4 (PB, RA), and W_5 (PB,RB) are investigated. In general, the main wheels have larger vibration than the plates. However, the plate has larger vibration at 7000 - 8500 Hz for W_1, 8000 - 10000 Hz for W_4, and 8000 - 14000 Hz for W_5. The main wheel and the plate have the same phase angle in the low frequency range. For W_1 and W_4, the phase lags begin to appear at about 10000 Hz, and they increase with the frequency. The phase lag of W_4 is slightly larger than that of W_1. However, W_5 does not have the phase lag in the measuring frequency range (0-20 kHz).

Regarding the theoretical prediction, the plate has larger vibration than the main wheel only at around f_{pr}. Also, the phase lags begin to appear at f_{pr}. When E_r is supposed to be 4.9×10^8 N/m^2, f_{pr}'s of W_1, W_4, and W_5 are 8900, 12600, and 20000 Hz, respectively. This theoretical prediction considerably agrees with the experimental results.

8.4.2 Rolling experiment

The amplitude of the rolling vibration strongly depends on the corrugation and the roughness of the contact surface of the wheels. Since the corrugation and the roughness increase with operating time, it is difficult to keep the surface conditions constant. In this experiment, the grooved wheel is used in order to compare the vibration amplitudes of various wheels.

Figures 8-8 and 8-9 show the vibrational accelaration and the noise, respectively. Comparing W_{st} and W_1 in Fig. 8-8, the absorber reduces the vibration by about 20 dB at the D, E, and F modes, and the total level is decreased by 16.5 dB. The theoretical prediction of the vibration reduction shown in Fig. 8-2 is 8 dB at the D mode, 13 dB at the E mode, and 8 dB at the F mode. These values are smaller than the experimental results, but decreasing tendencies correspond to each other.

As shown in Fig. 8-9, the noise is considerably decreased at the natural modes as well as the vibration, and the total level is decreased by 16.7 dB. Then, we can conclude that the damped wheel has enough effect in the noise reduction.

Concerning the damped wheel W_4 (PB, RA) and W_5 (PB, RA), the same experiments as W_1 were carried out. The results are similar to those of W_1.

8.5 Conclusions

In this chapter, the vibration of the damped wheel is theoretically analyzed under the assumption that the rubber is a spring with viscous damping which works only in the axial direction. To be precise, the damping in the circumferential and the radial derection should be taken into consideration. We also have to consider the frequency dependence of the rubber's Young's modulus and loss factor. However, in order to have the outline of the vibration and the noise abatements, the theoretical analysis mentioned in this chapter is useful. In this study, the absorber is attached on one side of the web. However, it

is possible to attach the absorbers on both sides. In this case, we can expect further abatement.

The following conclusions for the effective damped wheel are obtained.

i) The rubber coated wheel does not reduce the vibration, but the damped wheel composed of the main wheel, a thin annular plate and a rubber can reduce the vibration by about 20 dB.

ii) The rubber should have a large loss factor.

iii) The absorber should be attached to the outer side of the wheel.

iv) The vibration is remarkably decreased at the fundamental frequency of the absorber.

REFERENCES

1) Vér,I.L., et al., J.Sound & Vibration, 46-3 (1976), 395.

2) Matsumiya,S., & Sugawara,S., Sumitomo Kinzoku, 26-2 (1974), 97.

3) Arai,H., Proc.JSME, 810-18 (1981), 17.

4) Raquet,E., Rail Engineering International, January-March (1980), 13.

5) Satoda,K., et al., Sumitomo Kinzoku, 29-1 (1977), 68.

6) Sato,S., et al., Proc.JSME, 827-2 (1982), 100.

7) Mindlin,R.D., & Deresiewicz,H., J.Appl.Phys. 25-10 (1954), 1329.

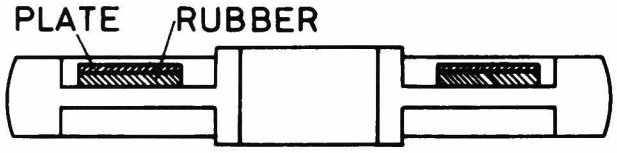

Fig. 8-1 Damped wheel.

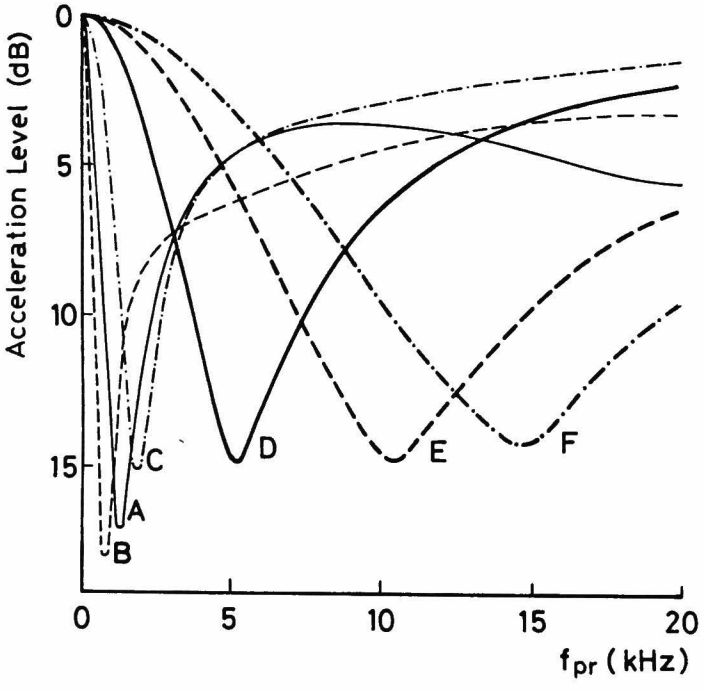

Fig. 8-2 Results of calculations on the relations between the acceleration levels and f_{pr}.

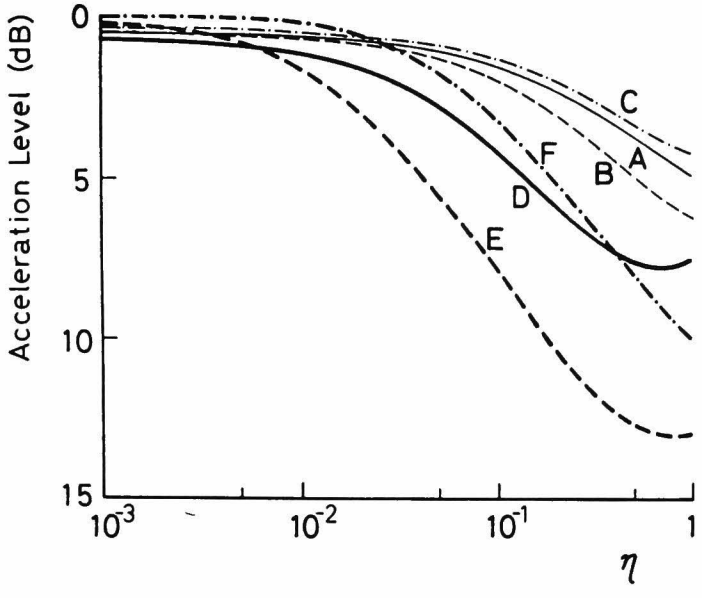

Fig. 8-3 Results of calculations on the relations between the acceleration levels and η.

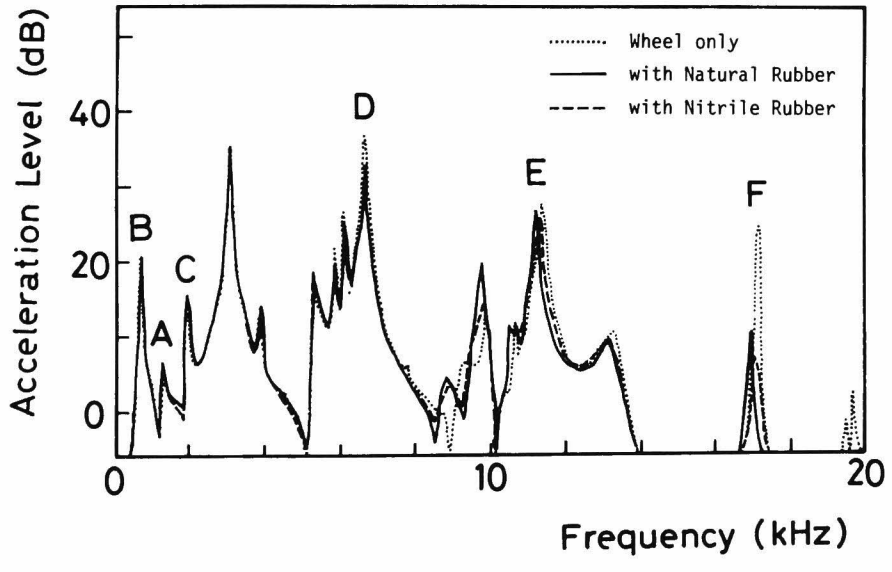

Fig. 8-4 Acceleration levels of the rubber coated wheels.

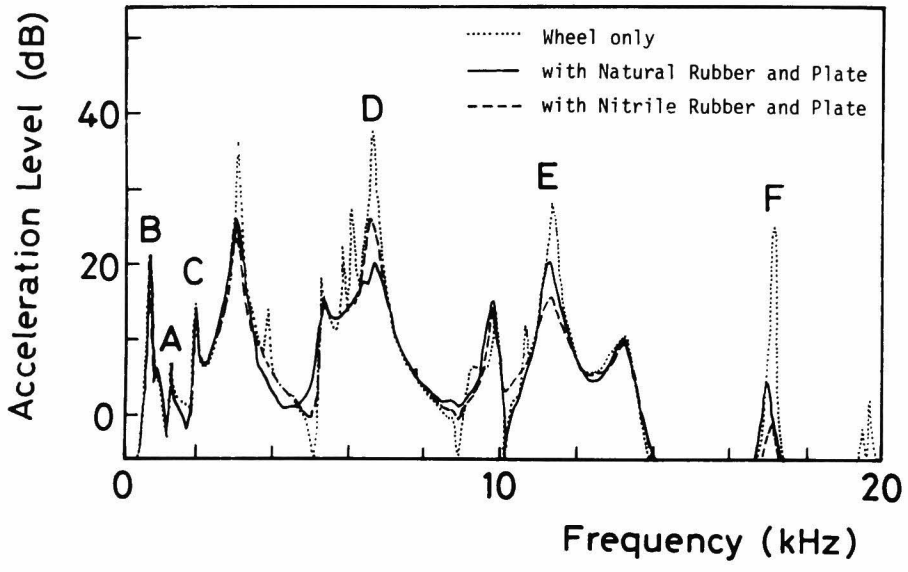

Fig. 8-5 Acceleration levels of the damped wheels with the natural and the nitrile rubbers.

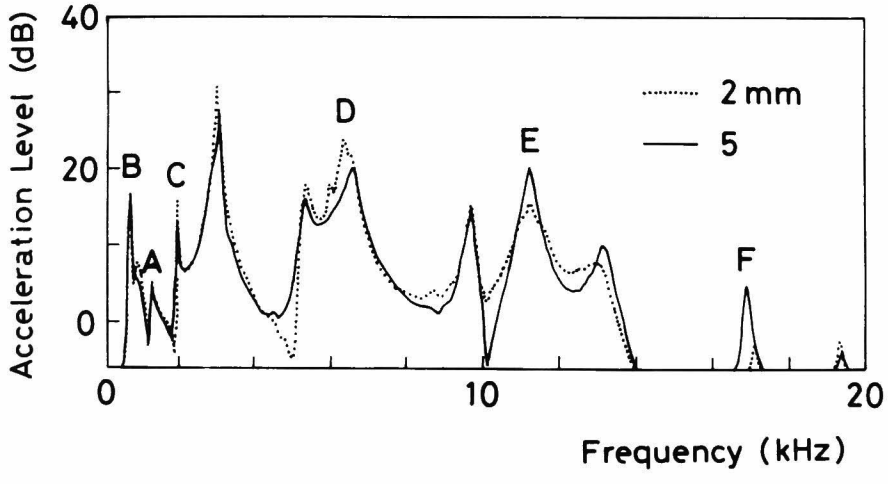

Fig. 8-6 Acceleration levels of the damped wheels with two kinds of rubber thickness.

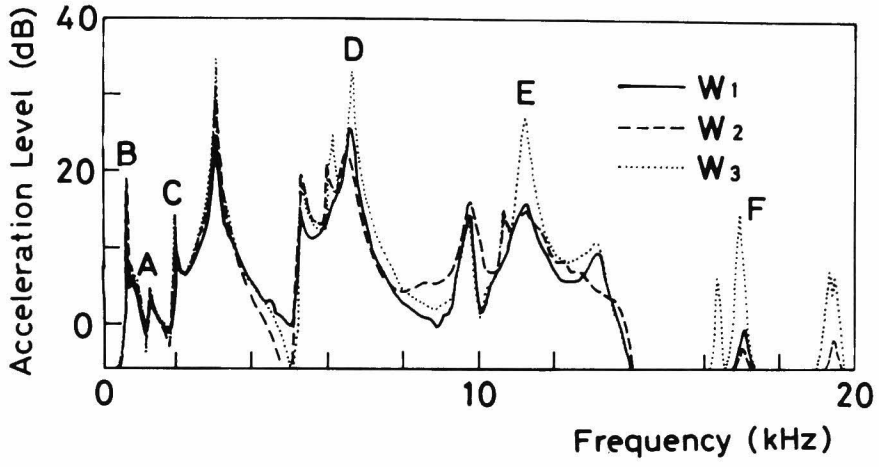

Fig. 8-7 Acceleration levels of the damped wheels with three kinds of damper's diameters.

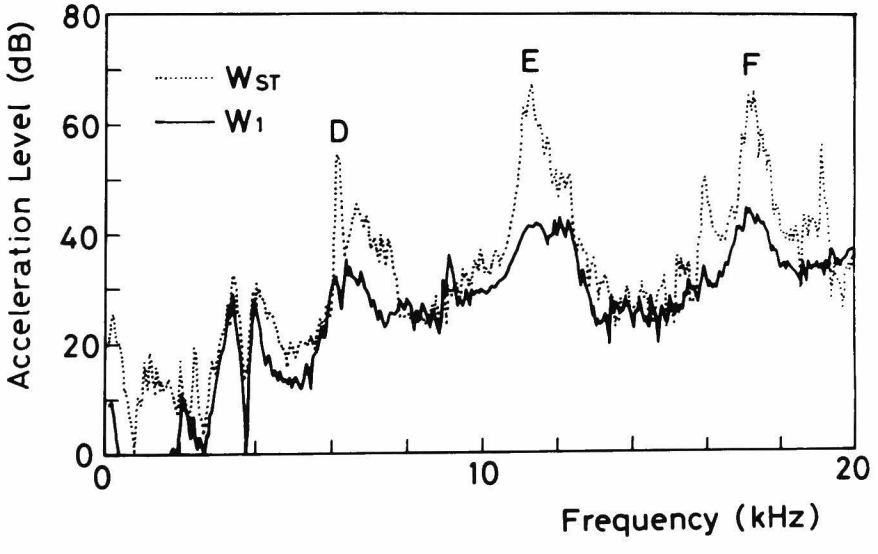

Fig. 8-8 Acceleration levels of the rolling damped wheel.

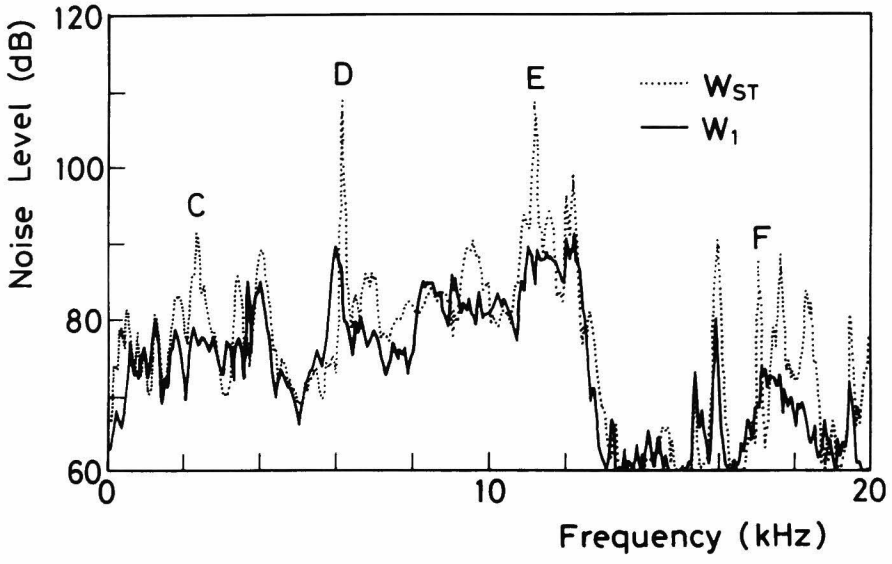

Fig. 8-9 Noise levels of the rolling damped wheel.

Table 8-1 Natural frequencies of the damped wheel.

	frequency (Hz)	mode (m,s)
A	1349	(0,0)
B	954	(1,0)
C	2305	(2,0)
D	6208	(3,0)
E	11300	(4,0)
F	17114	(5,0)

Table 8-2 Shapes of the rubber and the plate.

Rubber (r_1, r_2, h)	Plate (r_1, r_2, h)
RA (31,61,5)	PA (31,61,4)
RB (31,61,2)	PB (31,61,2)
RC (46,61,5)	PC (46,61,4)
RD (31,46,5)	PD (31,46,4)

Table 8-3 Theoretical acceleration levels of the damped wheel W_1, W_2, and W_3.

Mode	W_1	W_2	W_3
A	3.63	2.39	2.95
B	4.90	2.58	5.03
C	3.27	2.33	1.27
D	7.66	7.87	0.61
E	12.79	12.49	3.28
F	8.05	7.43	4.39

CHAPTER 9 CONCLUSIONS

The noise and the vibration generated by railways give a great deal of annoyance to the residents along the tracks, and their reduction is regarded to be of prime importance. In this work, the general concepts of the noise and vibration caused by the Shinkansen were investigated. Then, the transverse vibration of the wheel, which is one of the main sources of the noise, was analyzed theoretically and experimentally. Furthermore, noise reduction by using the spoke wheel and the damped wheel was investigated.

In chapter 2, the general concepts of the noise and the vibration caused by the Shinkansen was investigated by the measurements and questionnaires. The residents have been suffering from the noise and the vibration. For example, more than half of people who live very close to the track had headaches, and the houses were reported to have damages such as cracks in the wall and failures of the roof. From our investigation, we can say that the areas within 100 meters from the tracks are not suitable for comfortable living.

In chapter 3, the transverse vibration of the web wheel, which is commonly used in practical trains, was analyzed theoretically by making use of the Mindlin theory. The web wheel is simulated by a circular plate with a stepped thickness. The effects of shear deformation and rotatory inertia have important roles in the analysis, because the thickness of the rim is considerably large compared with the diameter.

In chapters 4 and 5, relations among the vibration, the noise, the rotational speed, the load, and the contact

angle were investigated. When the contact angle increases, the vibration and the noise which correspond to the normal modes of the transverse vibration increase. The vibration and the noise increase with the rotational speed. The load has influence on the spectra of the vibration and the noise, but does not have influence on their total levels. The very low order modes and the modes whose natural frequencies are near the coincidence frequency are important in the noise radiation, because they have large acoustic radiation coefficient which is defined by the ratio of the radiated sound power and the mechanical power of the vibrating wheel.

In chapter 6, the analytical method of the coupled vibration of the wheel and the rail was developed. Since the emphasis was placed on the wheel, the rail was simulated by a beam with free ends, and both were assumed to be connected by a spring. By improving the analysis of the rail and the coupling condition, however, this analytical method can be applied to the analysis of the practical wheel and rail.

In chapters 7 and 8, the analytical methods of the vibration of the spoke wheel and the damped wheel were developed, and their effects on the noise reduction were investigated experimentally. The spoke wheel can reduce the noise by several dB, and the damped wheel by about 20 dB. The noise reduction of the damped wheel depends on the structure of the absorber, and the guides for the optimum design were obtained. We can expect that the train noise is reduced considerably by using the spoke wheel and the damped wheel which can be used in practice from the viewpoint of mechanical strength and cost.

ACKNOWLEDGEMENTS

The auther would like to express his sincere gratitude to Professor Susumu Sato for his supervision and encouragement in the preparation of this thesis.

The author is also very grateful to Associate Professor Toshinobu Shibata for his valuable suggestions particularly on the vibration and noise by the Shinkansen.

Thanks are also extended to all the members of Laboratory of Vibration Engineering, Department of Precision Mechanics, Faculty of Engineering, Kyoto University for their helpful suggestions and discussions.